

HOPS-288: A Laboratory for Complex Organics in Proto-binary/multiple Systems

SHIH-YING HSU ,¹ NADIA M. MURILLO ,² CHIN-FEI LEE ,¹ DOUG JOHNSTONE ,^{3,4} TIEN-HAO HSIEH ,^{5,1}
 NAOMI HIRANO ,¹ LEONARDO BRONFMAN ,⁶ YO-LING CHUANG ,^{1,*} DAVID J. EDEN ,^{7,8} SHANGHOU LI ,^{9,10}
 SHENG-JUN LIN ,¹ MARK G. RAWLINGS ,¹¹ KEN'ICHI TATEMATSU ,^{12,13} SHENG-YUAN LIU ,¹ HUEI-RU VIVIEN CHEN ,¹⁴
 KEE-TAE KIM ,¹⁵ YI-JEHNG KUAN ,^{16,1} WOOJIN KWON ,^{17,18,19} CHANG WON LEE ,^{15,20} JEONG-EUN LEE ,²¹ TIE LIU ,²²
 QIUYI LUO ,^{23,24} PATRICIO SANHUEZA ,²⁴ AND HSIEN SHANG (尚賢)

¹*Institute of Astronomy and Astrophysics, Academia Sinica, No.1, Sec. 4, Roosevelt Rd, Taipei 106319, Taiwan (R.O.C.)*

²*Instituto de Astronomía, Universidad Nacional Autónoma de México, AP106, Ensenada CP 22830, B. C., México*

³*NRC Herzberg Astronomy and Astrophysics, 5071 West Saanich Rd, Victoria, BC, V9E 2E7, Canada*

⁴*Department of Physics and Astronomy, University of Victoria, Victoria, BC, V8P 5C2, Canada*

⁵*Taiwan Astronomical Research Alliance (TARA), Taiwan (R.O.C.)*

⁶*Departamento de Astronomía, Universidad de Chile, Casilla 36-D, Santiago, Chile*

⁷*Department of Physics, University of Bath, Claverton Down, Bath BA2 7AY, UK*

⁸*Armagh Observatory and Planetarium, College Hill, Armagh BT61 9DB, UK*

⁹*School of Astronomy and Space Science, Nanjing University, 163 Xianlin Avenue, Nanjing 210023, People's Republic of China*

¹⁰*Key Laboratory of Modern Astronomy and Astrophysics (Nanjing University), Ministry of Education, Nanjing 210023, People's Republic of China*

¹¹*Gemini Observatory/NSF NOIRLab, 670 N. A'ohoku Place, Hilo, HI 96720, USA*

¹²*Nobeyama Radio Observatory, National Astronomical Observatory of Japan, National Institutes of Natural Sciences, 462-2 Nobeyama, Minamisaku, Nagano 384-1305, Japan*

¹³*Astronomical Science Program, The Graduate University for Advanced Studies, SOKENDAI, 2-21-1 Osawa, Mitaka, Tokyo 181-8588, Japan*

¹⁴*Department of Physics and Institute of Astronomy, National Tsing Hua University, Hsinchu, 30013, Taiwan*

¹⁵*Korea Astronomy and Space Science Institute (KASI), 776 Daedeokdae-ro, Yuseong-gu, Daejeon 34055, Republic of Korea*

¹⁶*Department of Earth Sciences, National Taiwan Normal University, Taipei, Taiwan (R.O.C.)*

¹⁷*Department of Earth Science Education, Seoul National University, 1 Gwanak-ro, Gwanak-gu, Seoul 08826, Republic of Korea*

¹⁸*SNU Astronomy Research Center, Seoul National University, 1 Gwanak-ro, Gwanak-gu, Seoul 08826, Republic of Korea*

¹⁹*The Center for Educational Research, Seoul National University, 1 Gwanak-ro, Gwanak-gu, Seoul 08826, Republic of Korea*

²⁰*University of Science and Technology, Korea (UST), 217 Gajeong-ro, Yuseong-gu, Daejeon 34113, Republic of Korea*

²¹*Department of Physics and Astronomy, Seoul National University, 1 Gwanak-ro, Gwanak-gu, Seoul 08826, Korea*

²²*Key Laboratory for Research in Galaxies and Cosmology, Shanghai Astronomical Observatory, Chinese Academy of Sciences, 80 Nandan Road, Shanghai 200030, People's Republic of China*

²³*Institute of Astronomy, Graduate School of Science, The University of Tokyo, 2-21-1 Osawa, Mitaka, Tokyo 181-0015, Japan*

²⁴*Department of Astronomy, School of Science, The University of Tokyo, 7-3-1 Hongo, Bunkyo, Tokyo 113-0033, Japan*

Submitted to ApJ

ABSTRACT

Complex organic molecules (COMs) in young stellar objects (YSOs) have attracted significant attention in recent years due to their potential connection to pre-biotic chemistry and their utility as tracers of warm or shocked gas components. Proto-binary and multiple systems with close separations are particularly valuable targets for investigating chemical inheritance and reaction, as their members are expected to form from similar material in their parental cloud. We present ALMA observations of the hierarchical proto-triple system HOPS-288, focusing on the physical structure, kinematics, and COM compositions. The system is treated as a proto-binary system consisting of HOPS-288-A and HOPS-288-B due to the limited spatial resolutions, with a separation of 200 au. Three COM-rich features are revealed: two hot corinos associated with the two members, rich in a variety of COMs, and an intervening component between the two members traced by CH₃OH and tentatively by CH₃CHO. The hot corino in HOPS-288-A exhibits rotational features and might trace a disk.

The hot corino in HOPS-288-B is also possibly exhibiting rotational motion. The intervening component could possibly trace a shocked region in the circumbinary disk or a bridge between the two members. The column densities of COMs, including $^{13}\text{CH}_3\text{OH}$, CH_2DOH , CH_3CHO , HCOOCH_3 , $\text{C}_2\text{H}_5\text{OH}$, $^{13}\text{CH}_3\text{CN}$, and NH_2CHO , are broadly similar between the two sources, possibly suggesting the complex organic similarities among proto-binary/multiple systems. Given the complexity of the studied physical structures, further detailed investigations will be essential to confirm this result.

Keywords: Protostars — Complex organic molecules — Star formation — Astrochemistry — Pre-biotic astrochemistry

1. INTRODUCTION

Complex organic molecules (COMs) in young stellar objects (YSOs) have attracted significant attention in recent years due to their potential connection to prebiotic chemistry in subsequent planetary systems. COMs can be formed either on the icy mantles of dust grains and later released via desorption or directly in the gas-phase with previously desorbed parent molecules (see Ceccarelli et al. 2023, and the references therein). Gas-phase COMs are detected in YSOs at both the starless (e.g., Scibelli & Shirley 2020; Scibelli et al. 2024; Hsu et al. 2025) and protostellar stages (e.g., Belloche et al. 2020; Hsu et al. 2020; Yang et al. 2021; Hsu et al. 2022; Bouvier et al. 2022). In particular, the compact, warm regions enriched in COMs surrounding low- and intermediate-mass protostars are referred to as “hot corinos” (e.g., Ceccarelli 2004; Ospina-Zamudio et al. 2018). Hot corinos are generally attributed to heating of the innermost envelope by the central protostar (e.g., Ceccarelli 2004; Jacobsen et al. 2019; Hsu et al. 2023), although disk-origin hot corinos have also been reported (e.g., Lee et al. 2017). In addition to protostellar heating, shocks can also drive the release of COMs via localized ice sublimation and/or sputtering (e.g., Velusamy et al. 2002; Arce et al. 2008; Oya et al. 2016; Okuda et al. 2022; Hsu et al. 2023, 2024; Bouvier et al. 2025; Hsu et al. 2025). Because their presence requires efficient desorption mechanisms, COMs serve as valuable tracers of the morphologies and kinematics of either warm or shocked regions in protostellar environments (e.g., Jacobsen et al. 2019; Lee et al. 2019a; Hsu et al. 2025).

Several YSOs harboring COMs are simultaneously belonging to binary/multiple systems, such as IRAS 16293–2422, (e.g., Jørgensen et al. 2016, 2018; Manigand et al. 2020), L1551 IRS5 (Bianchi et al. 2020), L1448 IRS3B (Yang et al. 2021), Ser-emb 11 (Martín-Doménech et al. 2021), [BHB2007] 11 (Vastel et al. 2022), NGC 1333 IRS 4A (López-Sepulcre et al. 2017; Sahu et al. 2019; De Simone et al. 2020), SVS 13A (e.g., Bianchi et al.

2019; Yang et al. 2021; Bianchi et al. 2022; Hsieh et al. 2023b, 2024; Hsieh et al. 2025). Binary/multiple systems present more complex physical environments than single stars, involving intricate interactions among protostars (e.g., Pineda et al. 2012; van der Wiel et al. 2019), disks (e.g., Vastel et al. 2022), and outflows (e.g., Santangelo et al. 2015). In recent years, COMs have been recognized as valuable tracers for probing these environments in proto-binary/multiple systems. For example, in the proto-binary system [BHB2007] 11, Vastel et al. (2022) identified three CH_3OH components and proposed that two of them trace localized warm regions in the circumbinary disk, likely heated by mass-accretion streamers. Similarly, in the proto-binary system SVS 13A, Hsieh et al. (2024) concluded that COM emission cannot be explained by protostellar radiation alone, and that additional mechanisms, such as accretion shocks induced by large-scale infalling streamers, are likely at play.

Particularly for proto-binary/multiple systems with close separations (a few hundred au), the members are presumed to form from the same parental cloud and thus inherit comparable chemical ingredients. Accordingly, such systems are expected to host similar chemical compositions. However, direct comparisons of complex organic compositions within proto-binary/multiple systems remain challenging. First, for systems having merely a few hundred au, the emissions are difficult to distinguish. Meanwhile, the COM emission from YSOs can be weak due to the insufficient luminosity and gas density (Hsu et al. 2023) or be obscured by dust opacity (Sahu et al. 2019; De Simone et al. 2020). Despite these challenges, Bianchi et al. (2022) investigate the COM compositions between the two members of SVS 13 A, which has a separation of 90 au. Their evaluated column density ratios between the two sources are around 1 for CH_3OH , $^{13}\text{CH}_3\text{OH}$, and CH_3OCH_3 ; 2 for CH_3CHO ; and 4 for NH_2CHO . They suggested that the observed chemical segregation is likely due to the onion-like distribution of COMs. More investigations on the chemical compositions among the proto-binary/multiple systems are still desired.

HOPS-288 is a protostellar system cataloged by the Herschel Space Observatory (Furlan et al. 2016) and also

* Center of Astronomy and Gravitation, National Taiwan Normal University, 88 Sec.4 Ting-Chou Rd., Taipei 116, Taiwan, ROC

Table 1. Information of the spectral windows of the high-resolution data (#2018.1.01038.S) used in this study.

SPW	f_c	BW	df	dv	σ	Molecule
	(MHz)	(kHz)	(kHz)	(km s $^{-1}$)	(mJy beam $^{-1}$)	
#23	219552.6	60	31	0.042	7.3	C^{18}O
#29	218456.3	60	122	0.17	3.5	CH_3OH
#35	230529.7	938	488	0.64	2.5	CO, CH_3CHO , $\text{C}_2\text{H}_5\text{OH}$, and one CH_3OH line
#37	233491.8	1875	977	1.3	1.5	HCOOCH_3 , $\text{C}_2\text{H}_5\text{CN}$, NH_2CHO , and two CH_3OH lines

NOTE— f_c is the center frequency. BW is the bandwidth. df and dv are the spectral resolution and the corresponding velocity resolution, respectively. σ is the noise level.

observed with a target name of G211.47-19.27S under the project ALMA Survey of Orion PGCCs (ALMASOP; ALMA: Atacama Large Millimeter/sub-millimeter Array; PGCCs: Planck Galactic Cold Clumps; Dutta et al. 2020) and G211.47-19.27South in surveys such as Yi et al. (2018), Kim et al. (2020), and Tatematsu et al. (2021). Under the investigations of ALMASOP at 1.3 mm (230 GHz), this source was reported to be extremely rich in COMs (Hsu et al. 2020, 2022). High-resolution imaging from the VLA/ALMA Nascent Disk and Multiplicity (VANDAM) survey (Tobin et al. 2020) revealed that HOPS-288 is a binary system at 0.87 mm (345 GHz), HOPS-288-A and HOPS-288-B (hereafter source A and source B, respectively), with a separation of 200 au, and the former itself is a binary system having a separation of 50 au at 9 mm (33 GHz).

In this paper, we investigate the origin of COM emission in the HOPS-288 system and compare the COM compositions between its members. The two observational programs used in this study are introduced in §2. In §3, we examine the overall physical structure of the system, including the outflows and circumbinary disk. The COM morphologies and kinematics are presented in §4, providing insights into the origins of the observed COM emission. In §5, we derive the column densities and rotational temperatures of several molecules including COMs. We discuss the implications of our findings in §6 and summarize our conclusions in §7.

2. OBSERVATIONS

This study makes use of data obtained from two ALMA Cycle 6 programs: #2018.1.01038.S (PI: John Tobin) and #2018.1.00302.S (PI: Tie Liu). Both of them were observed in Band 6 (1.3 mm, 230 GHz). The former provides higher spatial resolution, while the latter covers wider bandwidth.

The high-resolution observation (#2018.1.01038.S) was carried out with the 12-m array only. The unprojected baselines spanned 11.6–1936 $\text{k}\lambda$, giving a maximum recoverable scale of $\sim 3''.7$. The targeted phase center was $(\alpha_{2000}, \delta_{2000}) = (05:39:56.0 - 07:30:27.6)$, and the absolute flux scale uncertainty is around 10%. The spectral setup

included eight SPWs with different resolutions; here we make use of SPWs #23, #29, #35, and #37, which cover CO, C^{18}O , CH_3OH , CH_2DOH , CH_3CHO , HCOOCH_3 , $\text{C}_2\text{H}_5\text{OH}$, and $\text{C}_2\text{H}_5\text{CN}$. Details of the bandwidths, spectral resolutions, and the corresponding molecular transitions are summarized in Table 1. Imaging was performed with `tclean` in CASA, with `robust = 0.5`. The synthesized beam was $\sim 0''.21$ (corresponding to 84 au at a distance of ~ 400 pc; Lombardi et al. 2011). The achieved sensitivity was ~ 0.19 mJy beam $^{-1}$ for the continuum (0.1 K at 230 GHz), while the per-channel sensitivities are listed in Table 1. Owing to its higher spatial and spectral resolutions, this dataset is primarily used to investigate the morphologies and kinematics of selected molecular tracers. We summarize the transition information in Table A1.

The wide-bandwidth (#2018.1.00302.S) data employed ALMA the 12-m array. The unprojected baselines ranged from 11.6 to 1075 $\text{k}\lambda$, corresponding to a maximum recoverable scale of $\sim 3''.7$. The targeted phase center was [05:39:56.1 – 07:30:28.4], and the absolute flux scale uncertainty is around 10%. The four spectral windows each had a bandwidth of 1,875 MHz and a spectral resolution of 1.129 MHz (~ 1.4 km s $^{-1}$ at 230GHz). Imaging was performed with `tclean` in CASA (CASA Team et al. 2022), adopting a Briggs robust parameter of 0.5. The resulting synthesized beam was $\sim 0''.37$ (corresponding to ~ 148 au at a distance of ~ 400 pc; Lombardi et al. 2011). The achieved sensitivities were ~ 0.64 mJy beam $^{-1}$ for the full-band continuum (0.13 at 230 GHz) and ~ 3.6 mJy beam $^{-1}$ per channel. Given its broad spectral coverage, this dataset is primarily used for deriving chemical compositions. We summarize the transition information in Table A2.

The visibility data of both observations have been applied the self-calibration of phase using the initially exported continuum multi-frequency synthesis image. The calibration tables were obtained by `gaincal` with infinite solution interval. The calibration were applied to the visibility data by `applycal` with linear interpolation. In the high-resolution observations, the dust-continuum peak flux density increased

by 50% and the signal-to-noise ratio (SNR) by a factor of three. In the wide-coverage observations, the corresponding increases were 3% and 25%. For the continuum-subtracted data cubes, the line flux density and its SNR in the high-resolution observations improved by around ten percent, whereas the corresponding improvements in the wide-coverage observations were a few percent.

Since neither of the two data sets resolves the local binarity of source A, in this study we treat source A as a single system. The position is set at the peak of the unresolved dust continuum at source A.

3. PHYSICAL STRUCTURE OF THE MULTIPLE SYSTEM

We first investigated the physical structures of the system using the high-resolution (#2018.1.01038.S) data.

3.1. Dust

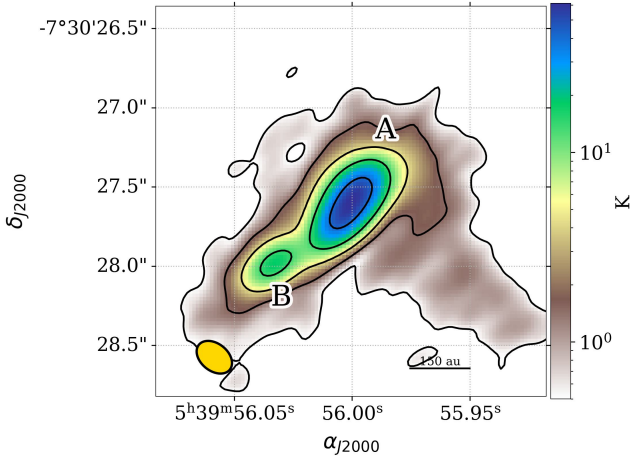


Figure 1. 1.3 mm dust continuum observed by the high-resolution data. The contour levels are $[5, 15, 45, 135, 405]\sigma$, where σ is 0.10 K. The yellow ellipse at the bottom left corner illustrates the beam. The texts “A” and “B” label the two continuum peaks.

Figure 1 presents the 1.3 mm dust continuum from the high-resolution (#2018.1.01038.S) data. The lowest contour (5σ) is elongated and encompasses both source A and source B, possibly tracing a circumbinary disk surrounding the system. Such a flattened morphology suggests that the system may be oriented close to edge-on. The third-lowest contour (32σ) appears to trace the localized structure of each source more distinctly. At the positions of source A and source B, the continuum emission shows slight elongation, which may correspond to individual circumstellar disks around each source. The dust continuum emission is seen to extend southwest from the system. Further self-calibration could improve the sensitivity and potentially reveal this structure more clearly, although such refinements are beyond

the scope of the present work. We applied 2D Gaussian fitting on the dust continuum image and summarize the 2D Gaussian fitting results in Table 2. For completeness, we show the comparisons of the 1.3 mm dust continuum images from both high-resolution (#2018.1.01038.S) and wide-bandwidth (#2018.1.00302.S) in Figure B1.

3.2. Outflows

Figure 2 presents the integrated intensity (moment 0) and intensity-weighted mean velocity (moment 1) images of the CO $J = 2 - 1$ transition overlaid with the 1.3 mm dust continuum. As shown in Figure 2 (a), the moment 0 image of CO reveals outflows launched from both source A and source B, particularly visible on the southwestern side of the system. The orientations of the outflows are consistent with the minor axes (i.e., perpendicular to the major axes) of their originated sources. Also, the southwestern extension of the dust continuum illustrated by the black solid contours possibly traces the cavity wall of source A’s outflow, similar to the case of L1551 IRS 5 (Sabatini et al. 2025).

At the southwestern side, the outflow from source A clearly exhibits a wider opening angle than that from source B. Due to the slight difference in axis orientation between the two sources, the outflows overlap in the northeastern region, making the outflow lobes there hardly distinguished. To better distinguish the outflow lobes in the northeastern region, we plot the CO $J = 2-1$ integrated intensity contours for the red- and blue-shifted channels separately. As shown in Figure 2(a), the cavity wall of source A’s outflow can be clearly identified in the northeastern region, whereas the cavity of source B’s outflow remains unclear.

The different opening angles may suggest that source A is at a more advanced evolutionary stage (e.g., Hsieh et al. 2023a; Dunham et al. 2024). Alternative explanations for the wide-opening morphology of source A, considering the binarity of source A, include the presence of two outflows (e.g., NGC 1333 IRAS 4A; Santangelo et al. 2015) or jet precession (e.g., Raga et al. 2009; Louvet et al. 2018). Additional support for an evolutionary difference between source A and source B comes from the (non-)detection of collimated SiO jets. SiO jets are typically observed in Class 0 rather than Class I protostars, though a few detections in Class I objects have been suggested (Dutta et al. 2022). Dutta et al. (2024) detect a collimated SiO $J = 5-4$ jet only from source B (see also Figure B1). This supports that source A is more evolved, whereas a possible weak jet indicated by the compact SiO emission detected at source A remains unconfirmed.

Finally, as shown in Figure 2(b), the outflows from source A and source B are predominantly blueshifted and redshifted, respectively. The relatively uniform speed within each outflow suggests that they are viewed close to edge-on.

Table 2. The 2D Gaussian fitting results of the dust continuum of the two sources.

Source	RA	DEC	Image Size	Deconv. size	F_ν	I_ν^{peak}
	(J2000)	(J2000)	(MAJ, MIN, PA)	(MAJ, MIN, PA)	(mJy)	(mJy beam $^{-1}$)
HOPS-288-A	05:39:56.00	−07:30:27.6	0''.44, 0''.25, 141°	0''.40, 0''.19, 144°	278	78
HOPS-288-B	05:39:56.03	−07:30:28.0	0''.34, 0''.20, 116°	0''.27, 0''.13, 116°	51	23

NOTE— Deconv. size is the image component size deconvolved by the beam. I_ν^{peak} is the peak specific intensity. F_ν is the flux density.

3.3. Circumbinary Disk

Figure 3(a) presents the integrated intensity map of C^{18}O (color scale) overlaid with the 1.3 mm dust continuum (black contours). The C^{18}O emission shows three bright components distributed from southeast to northwest: (i) one covering the southeast side of the dust continuum, (ii) one located in the gap between source A and source B, and (iii) one covering the northwest side of the dust continuum, which, similar to the dust, extends toward the southwest. The morphology, with C^{18}O lying along the midplane and flanking both sides of the elongated dust continuum, suggests that the two C^{18}O component (i) and (iii) are possibly tracing the circumbinary disk.

To model the possible disk motion, we extracted a position–velocity (PV) diagram along the cut penetrating source A and B ($\text{PA} = 127^\circ$), as indicated by the purple line in Figure 3(a). The resulting PV diagram is shown in Figure 3(b), with the reference position set at the gap between source A and source B. The reference velocity, defined as the system velocity of the circumbinary disk v_{CBD} , was set at 5.0 km s^{-1} based on the best symmetry of the PV diagram.

The PV diagram shown in 3(b) reveals three features located at $\Delta p = +0''.75$, $0''.0$, and $-0''.75$, corresponding to the three bright components from southeast to northwest in Figure 3(a). The features at $\Delta p = +0''.75$ and $-0''.75$ correspond to the red- and blueshifted sides of the circumbinary disk, respectively. Note that the red- and blueshifted motion are consistent with that observed in the CO outflow in Figure 2(b).

We assumed that the circumbinary disk follows Keplerian rotation around a central mass (M_{cen}) as $v = (GM_{\text{cen}}/R)^{1/2}$, where R is the radius. Based on the spatial extent of the blueshifted component at $\Delta p = -0''.75$, we adopt an outer radius of $1''.25$ (500 au) for the circumbinary disk. We constructed a grid of parameters by varying the central mass (M_{cen}) from 1 to $10 M_\odot$ in steps of $0.25 M_\odot$. We also varied the inclination angle (φ), defined such that 90° corresponds to a perfectly edge-on geometry, between 75° and 105° in steps of 5° . The fitting was evaluated by the sum of squared error between the relative velocity (Δv) at each relative position (Δp). The observed velocity was

evaluated by the maximum value of 5σ , as indicated by the red and blue markers in Figure 3(b).

The best-fit central mass (M_{cen}) is $5.00 M_\odot$ for an edge-on orientation ($\varphi = 90^\circ$), $5.25 M_\odot$ for a tilt of 5° and 10° , and $5.50 M_\odot$ for a tilt of 15° . The best-fit velocities at different inclination angles are shown by the cyan and magenta markers in Figure 3(b). All of these best-fit models can describe the observations well. The relatively high mass suggests that this system is an intermediate-mass protostellar system, which is broadly consistent with its reported high luminosity ($180 \pm 70 L_\odot$, Dutta et al. 2020; Hsu et al. 2022), though we note that luminosity can also have an accretion component.

4. MORPHOLOGY AND KINEMATICS OF COMPLEX ORGANICS

4.1. Morphology of Methanol

CH_3OH is the simplest and most commonly detected COM and is frequently used as a tracer of complex organic chemistry. Figures 4(a)–(d) show CH_3OH transitions with upper energy levels ranging from $E_u = 45 \text{ K}$ to 683 K , revealing similar structure with apparent variations. At $E_u = 45 \text{ K}$, Figure 4(a), the morphology exhibits a hamburger-like morphology covering the dense continuum structure. In addition, we identify an intervening component that appears to form a tail connecting the two sources. The hamburger- and tail-like morphologies gradually become unclear with increasing upper energy levels, as seen by comparing Figure 4(a) to (d). At $E_u = 683 \text{ K}$, Figure 4(d), two compact CH_3OH components become prominent. The two components locate at the positions of source A and source B, suggesting that both sources host their own hot corinos.

The hot corino associated with source A exhibits a dark lane sandwiched by two bright features in Figures 4(a)–(d), forming a hamburger-like morphology. The dark lane likely arises from the midplane material that has relatively low temperature and high optical depth. In addition, the northeastern layer is brighter than the southwestern one. Given that the system is likely viewed near edge-on, the CH_3OH emission may originate from the upper and lower

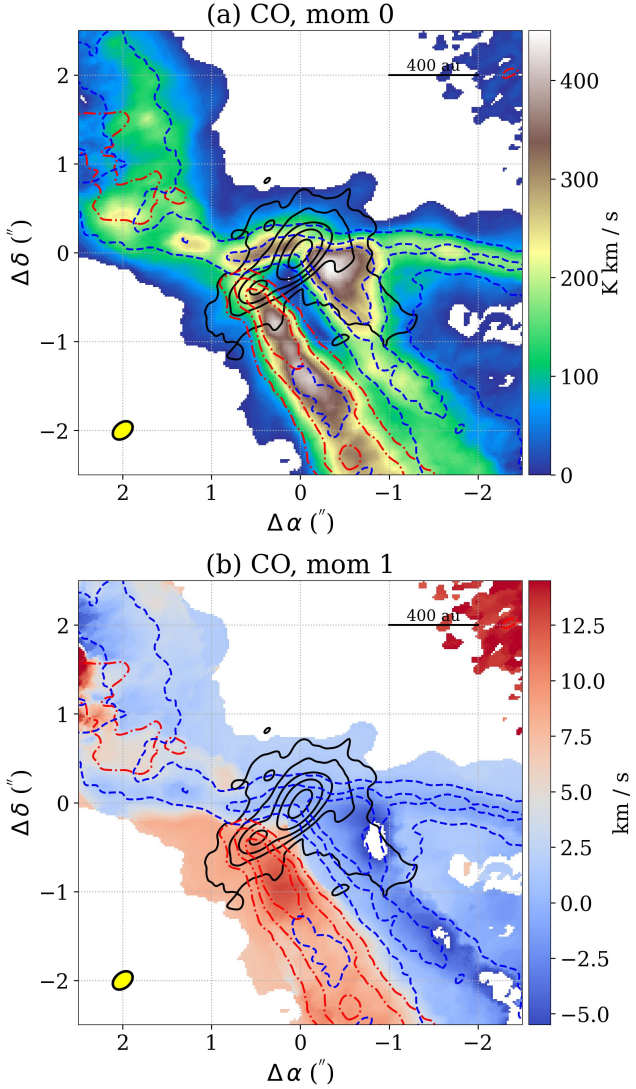


Figure 2. (a) Integrated intensity and (b) intensity-weighted mean velocity maps of CO $J = 2-1$, overlaid with 1.3 mm dust continuum (black solid contours) and CO $J = 2-1$ integrated intensity in red-shifted (red dash-dotted contours) and blue-shifted (blue dashed contours) velocity channels. All the data were obtained from the high-resolution observations. For panel (a), the integration interval was from -15 to 25 km s^{-1} . A mask of 5σ was applied during the integration. The black contours are at $[5, 15, 45, 135, 405]\sigma$, where σ is 0.10 K. The velocity intervals of the red dash-dotted and blue dashed contours are $[+10, +25]$ and $[-15, 0]$ km s^{-1} , respectively. Both are at $[10, 30, 50]\sigma$, where σ is 5.64 K km s^{-1} . The origin of the coordinates is set to the position of source A.

surfaces of a disk. The emission is brighter in the northeast likely because the disk is tilted slightly to the southwest, allowing us to observe the warmer inner region of the upper surface. This could be similar to the disk atmosphere case of HH 212 (Lee et al. 2017, 2019a). To confirm this as well as the origin of the unresolved hot corino in source B,

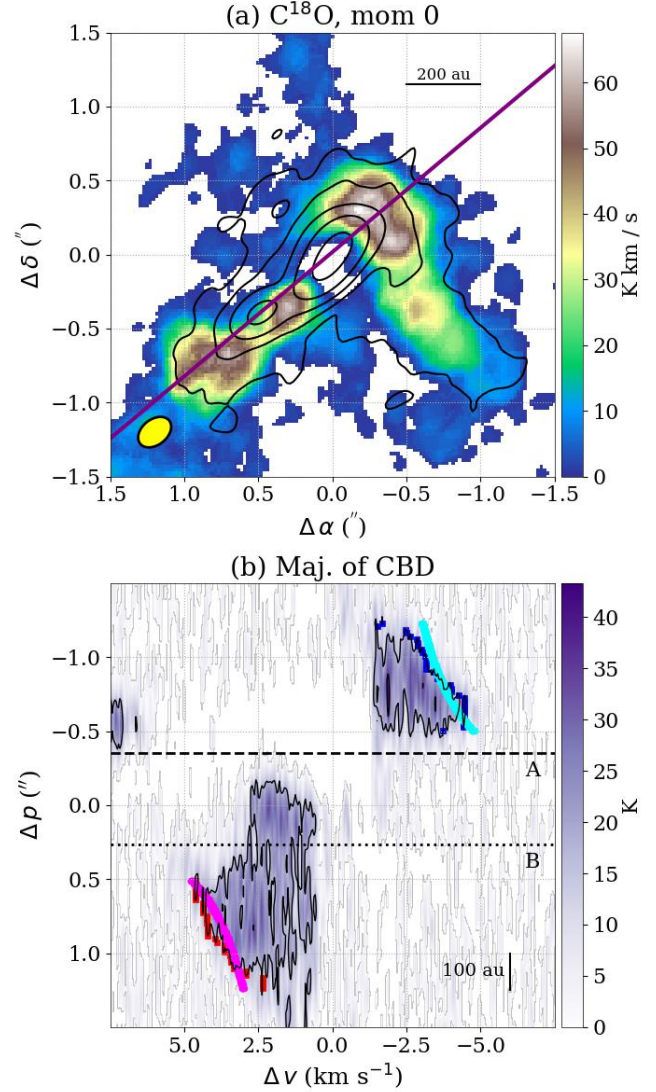


Figure 3. Integrated intensity image (a) and PV diagram (b) of the C^{18}O $J = 2 - 1$ transition from high-resolution observations. The black contours in (a) show the 1.3 mm continuum at $[5, 15, 45, 135, 405]\sigma$. Coordinates in panel (a) is centered on source A. A mask of 5σ was applied during the integration. The PV diagram (b) is extracted along the circumbinary disk axis illustrated by the purple line in panel (a). The black contour in (b) shows the 5σ of C^{18}O emission. The reference velocity ($\Delta v = 0$ km s^{-1}) of the PV diagram is set to 5 km s^{-1} . The reference position ($\Delta p = 0$ km s^{-1}) was set at the gap between source A and source B ($5:39:56.02, -7:30:27.8$). The red and blue markers represent the datapoints used for fitting the rotation motion of the C^{18}O gas component. The magenta and cyan markers show the modeling results.

we investigate the kinematics of CH_3OH in the next section (Section 4.2). We note that the hot corino in source A shows a small offset ($0''.05$) toward the northwest from its continuum peak, indicating an asymmetric structure within source A.

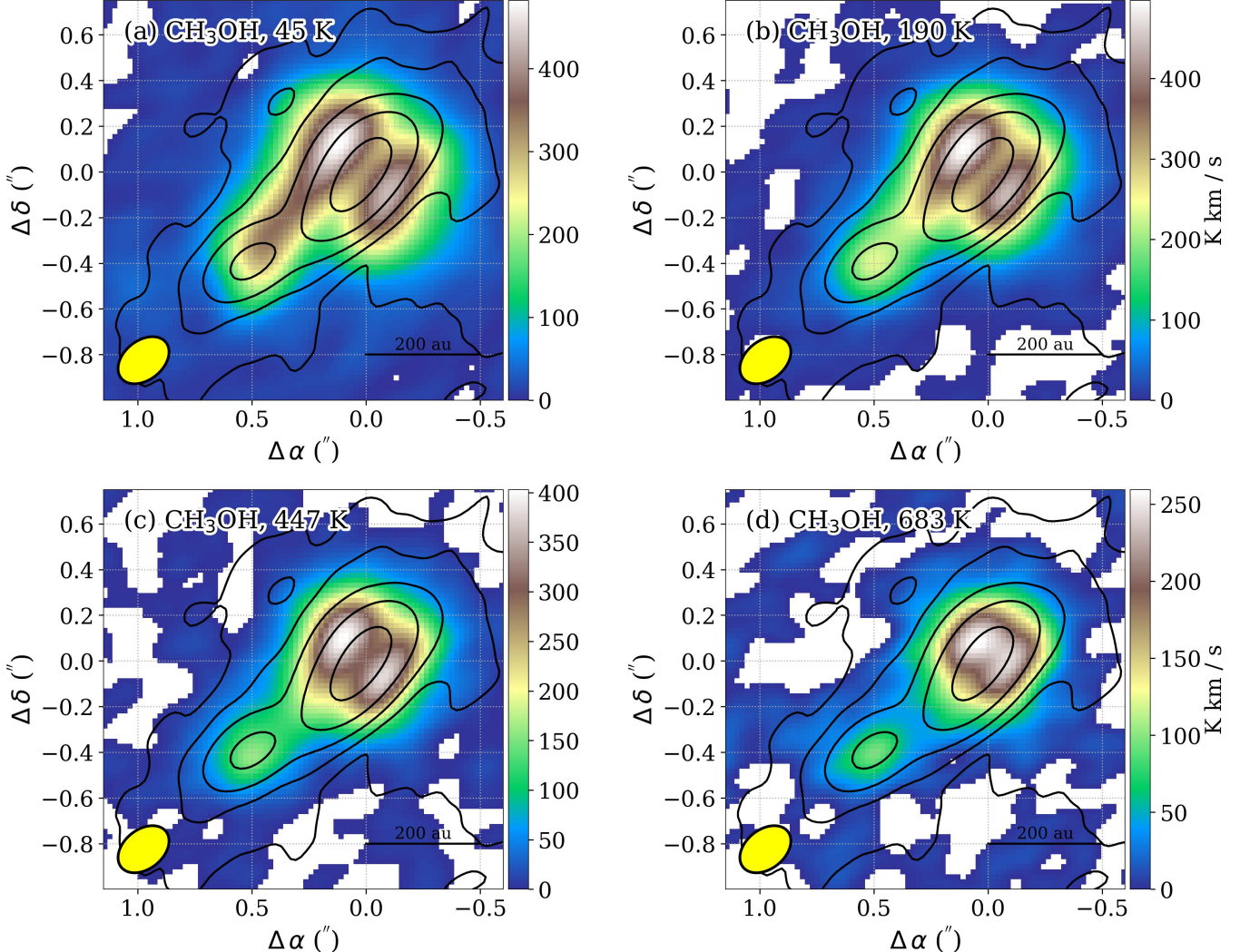


Figure 4. The integrated intensity images of CH_3OH transitions overlaid with dust continuum (black contours at $[5, 15, 45, 135, 405]\sigma$ and $\sigma = 0.10 \text{ K}$). The integration intervals span from -2.5 to $+12.5 \text{ km s}^{-1}$.

The intervening component that appears as a tail connecting the two sources in Figure 4(a) could represent a physical bridge between them, although we cannot rule out the possibility that this structure is an artifact caused by beam convolution. If the tail-like morphology is indeed artificial, the presence of the intervening emission would instead suggest a localized warm or shocked region in the vicinity of source B. The absence of this component in the higher- E_u transition further indicates that it is cooler than the two individual hot corinos.

4.2. Kinematics Revealed by Methanol

To investigate the kinematics of the COM-rich gas components, we extracted PV diagrams of CH_3OH along the major axis of each source. The cuts (“Maj. of A” and “Maj. of B”) are illustrated in Figure 5 and the PV diagrams are presented in Figure 6. Two additional cuts,

“Maj. of CBD” and “Tail,” indicated in Figure 5, are also used for the analyses discussed in the following sections. The reference velocities of the PV diagrams ($\Delta v = 0 \text{ km s}^{-1}$) for each cut were set to maximize symmetry based on the lowest upper energy transitions, namely Figure 6(a) and (e) for source A and source B, respectively. The values are 3.5 and 6.5 km s^{-1} for source A and source B, respectively. We chose these transitions because they have the best spectral resolution and the strongest line intensities among our data. The reference positions correspond to the continuum peak of each source.

Figure 6(a) presents the PV diagram along the major axis of source A for the $\text{CH}_3\text{OH} E_u = 45 \text{ K}$ transition. A clear linear correlation between Δp and Δv , indicated by the black dashed line selected by visual inspection, suggests that the gas traces a localized rotational structure, possibly a ring or disk. In the upper-right quadrant ($\Delta v < 0 \text{ km s}^{-1}$, $\Delta p <$

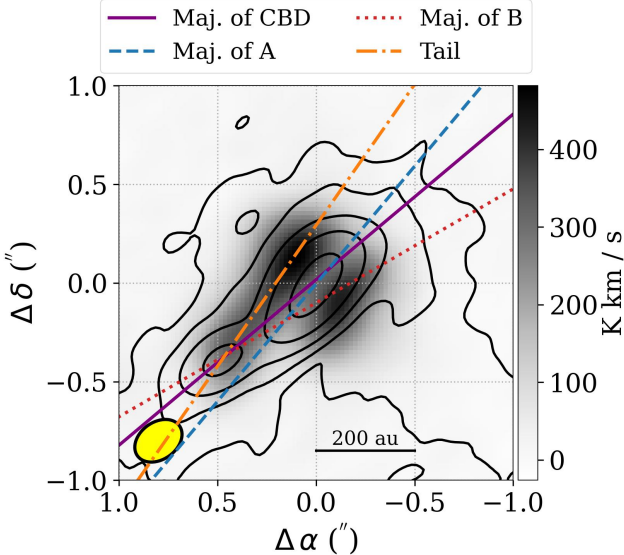


Figure 5. The cuts used in this study overlaid on integrated intensity image of CH_3OH 4_{2,3} – 3_{1,2} ($E_u = 45$ K) transition (color scale). The image is also overlaid by 1.3 mm continuum (black contours at $[5, 15, 45, 135, 405]\sigma$ and $\sigma = 0.10$ K).

$0''$), the blueshifted emission exhibits a characteristic of disk motion (e.g., Lee et al. 2017). However, the corresponding redshifted component on the opposite side, expected at $0'' < \Delta p < 0''.5$, is absent in Figure 6(a). As shown in Figure 6(c) and (d), the redshifted component gradually becomes visible at $\Delta p = 0''.2$ and $\Delta v = 4 \text{ km s}^{-1}$. At higher- E_u transitions the redshifted component remains much fainter than the blueshifted side. This discrepancy is consistent with the offset we observed in the morphology, Figure 4 and described in Section 4.1).

The second row of Figure 6 presents the PV diagrams along the major axis of source B for the four CH_3OH transitions. In Figure 6(e), the black dashed line highlights a tentative linear correlation, indicative of rotational motion in the CH_3OH gas. Given the limited spatial resolution, we cannot determine whether this structure corresponds to an unresolved ring or disk. An offset peak appears at $\Delta v = +0.00 \text{ km s}^{-1}$ and $\Delta p = -0''.1$, which is likely associated with the intervening component, as it disappears in the higher- E_u transitions shown in Figures 6(f), (g), and (h). As this component diminishes, the hot corino emission in source B becomes increasingly apparent. Its peak position, at $\Delta v = -1 \text{ km s}^{-1}$ and $\Delta p = -0''.1$, is slightly blueshifted and offset from the continuum peak ($\Delta p = 0''$).

We further model the rotation motion for source A and source B, which are based on the black dashed lines in Figures 6(a) and (e). The black dashed lines, selected by visual inspection, are intended to illustrate the linearity. The

linearity between Δp and Δv can be described as:

$$\left(\frac{\Delta p}{0.50 \text{ arcsec}} \right) = \left(\frac{\Delta v}{5 \text{ km s}^{-1}} \right) \quad (1)$$

for source A and

$$\left(\frac{\Delta p}{0.10 \text{ arcsec}} \right) = \left(\frac{\Delta v}{5 \text{ km s}^{-1}} \right) \quad (2)$$

for source B. Assuming that the disk mass is much smaller than the stellar mass and an edge-on geometry, the relative velocity along the line of sight (Δv) at a relative position (Δp) following of a Keplerian rotation is:

$$\Delta v = \sqrt{\frac{GM_\star}{R}} \frac{\Delta p}{R}, \quad (3)$$

where M_\star and R are the stellar mass and rotation radius, respectively. Given a distance of 400 pc (Lombardi et al. 2011) and adopting the outer boundaries of the PV diagrams as the sizes of the rotating features, 200 au ($0''.50$) for source A and 40 au ($0''.1$) for source B, the inferred stellar masses are $2.9 M_\odot$ for source A and $1.1 M_\odot$ for source B. The sum of the two stellar masses ($4.0 M_\odot$) is comparable to the value ($\sim 5.00 M_\odot$) estimated from the circumbinary disk motion traced by C^{18}O in Section 3.3.

Regarding the kinematics of the intervening component, Figure 7 shows the PV diagrams of C^{18}O (color scale) and CH_3OH 45 K transitions (contours) along the tail. The contour levels start from 20σ , rather than 5σ , to better visualize this component. The cut passes through the source B continuum peak, as illustrated by the orange dash-dotted line in Figure 5. As shown in Figure 7, a localized enhancement, previously observed in Figure 6(e), is present at $\Delta p = 0''.5$ (green arrow). This component appears to coincide with the inner part of the redshifted portion of the circumbinary disk traced by C^{18}O , as suggested by the location and velocity of this component. This may indicate a localized heated and/or shocked region in the circumbinary disk. The potential origins of such a feature include mass flow from source A to source B or an accretion streamer from the surrounding medium. A detailed modeling that incorporates accretion flows will be necessary for further confirmation.

4.3. Diversities and Similarities between Complex Organics

Similar morphologies and kinematics are seen in other COMs, although some differences between those of COMs are present. In Figure 8, we present integrated intensity maps for selected COM transitions, while Figure 9 shows the corresponding PV diagrams taken along the major axis of the circumbinary disk. For CH_2DOH , CH_3CHO , HCOOCH_3 , $\text{C}_2\text{H}_5\text{OH}$, $\text{C}_2\text{H}_5\text{CN}$, multiple transitions were stacked to improve the signal-to-noise ratio (SNR). In the PV diagrams

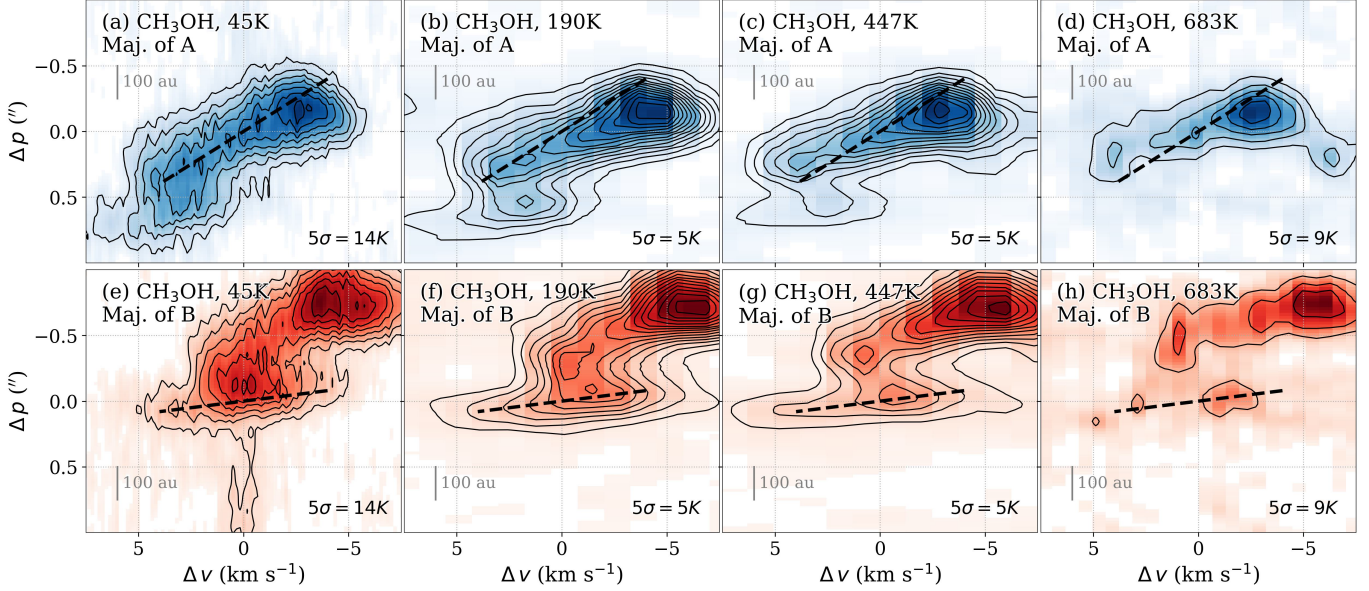


Figure 6. PV diagrams along the major axes of source A and source B. Contours start at 5σ and increase in steps of 5σ . The reference velocities ($\Delta v = 0 \text{ km s}^{-1}$) were set to 3.5 and 6.5 km s^{-1} for source A and source B, respectively, chosen to maximize the symmetry of the diagrams. The reference positions ($\Delta p = 0 \text{ km s}^{-1}$) were set to the positions of source A and source B for the top and bottom rows, respectively. The black dashed lines illustrate the velocity gradient relations derived from panel (a) and (e) for the top and bottom rows, respectively.

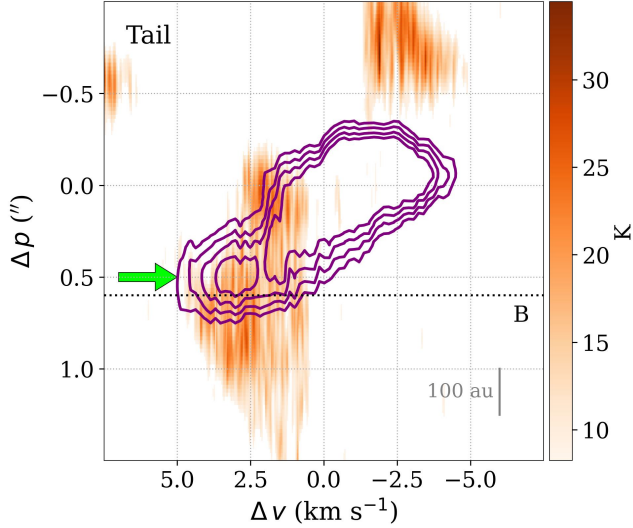


Figure 7. PV diagrams of the C^{18}O (color scale) and CH_3OH 45 K transitions (contours) extracted along the tail-like feature. The reference velocity ($\Delta v = 0 \text{ km s}^{-1}$) is set to 5 km s^{-1} . The reference position ($\Delta p = 0 \text{ km s}^{-1}$) is set to the position of source A. Contours expand between 20σ and 35σ in steps of 5σ . The green arrow points to the localized enhancement.

(Figure 9), the reference velocity ($\Delta v = 0 \text{ km s}^{-1}$) is set to 5 km s^{-1} , corresponding to the systemic velocity derived from the rotation of the circumbinary disk. The reference position is fixed at the location of source A, while source B appears at $\Delta p = 0''.6$. Cyan and magenta dashed lines indicate the best-fit velocity structures for source A

and source B, respectively, obtained from the CH_3OH PV diagrams with the methods described Section 4.2. Since the major axis of the circumbinary disk differs only slightly (10°) from those of source A and source B, these modeled correlations (Equations 1 and 2) remain robust and provide useful insights on the overall kinematics. For comparison, panels (a) and (b) in both Figure 8 and Figure 9 present the CH_3OH transitions with $E_u = 45 \text{ K}$ and 447 K , respectively.

The morphologies of CH_2DOH , CH_3CHO , HCOOCH_3 , $\text{C}_2\text{H}_5\text{OH}$, $\text{C}_2\text{H}_5\text{CN}$, and NH_2CHO all exhibit two distinct hot corinos, as shown in Figures 8(c)–(h). The tail structure is generally absent, except for CH_3CHO , where the tail feature tentatively appears at the top atmosphere in Figure 8(d). This suggests that, for these COMs, the observed emission is dominated by the individual hot corinos of the two sources. Consistently, as shown in Figures 9(c)–(g), the PV diagrams of CH_2DOH , CH_3CHO , HCOOCH_3 , $\text{C}_2\text{H}_5\text{OH}$, and $\text{C}_2\text{H}_5\text{CN}$ (i.e., all the other COMs excepting NH_2CHO) are similar with that of CH_3OH 447 K in 9(b).

One exception is NH_2CHO . As shown in Figure 9(h), the diagram does not follow the typical linear relation between Δp and Δv observed for the other COMs. However, based on the contour shapes and the relative Δp positions of the intensity peaks, we can still identify that the blueshifted and redshifted components are slightly offset toward the northwestern and southeastern sides of the continuum peak ($\Delta p = 0''$), respectively, consistent with the overall rotation of the system. These characteristics suggest that NH_2CHO resides in the more inner part ($0''.1$ in Figure 9(h)) of source A, which is further supported by its limited spatial extent

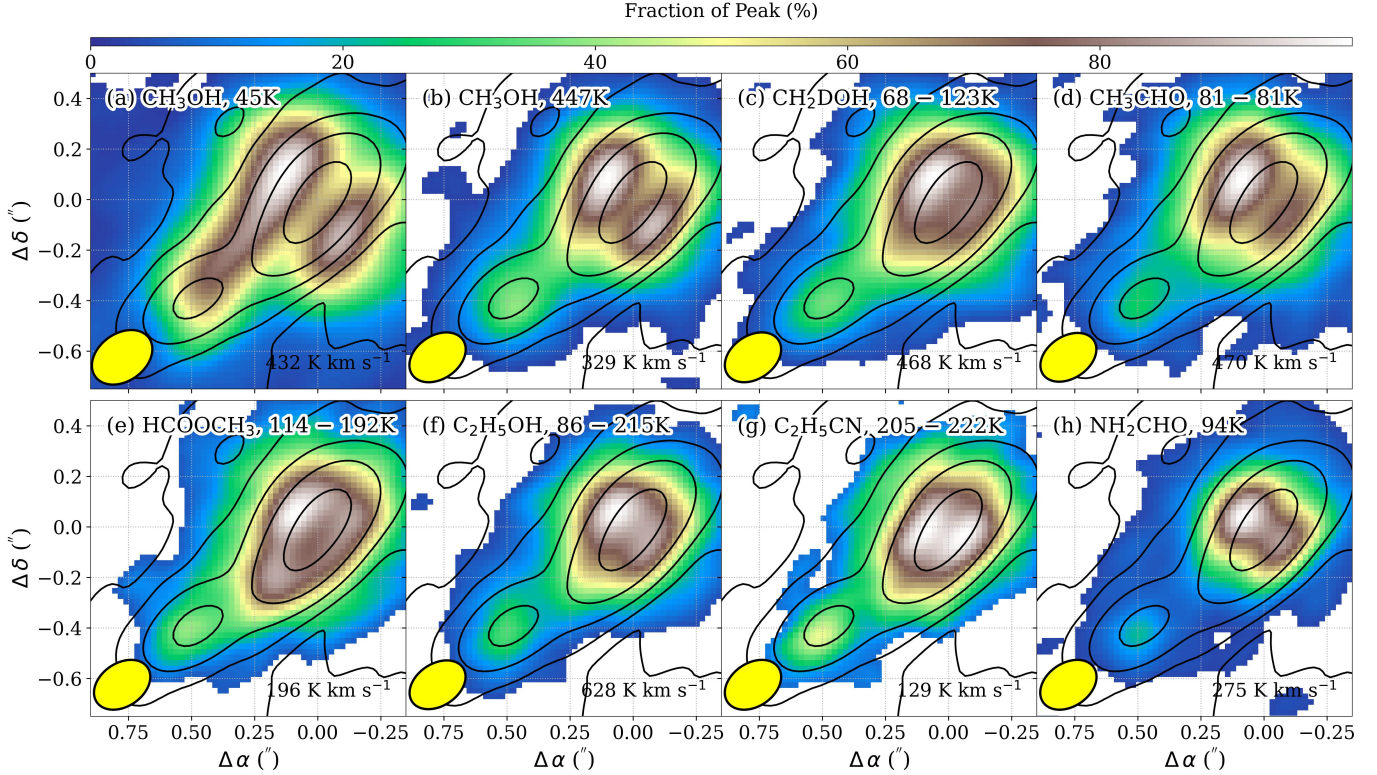


Figure 8. The integrated intensity images of selected COM transitions (color scale) overlaid with continuum (black contours at [5, 15, 45, 135, 405] σ and $\sigma = 0.10$ K). The velocity range for integration is fixed to [0, 10] km s $^{-1}$.

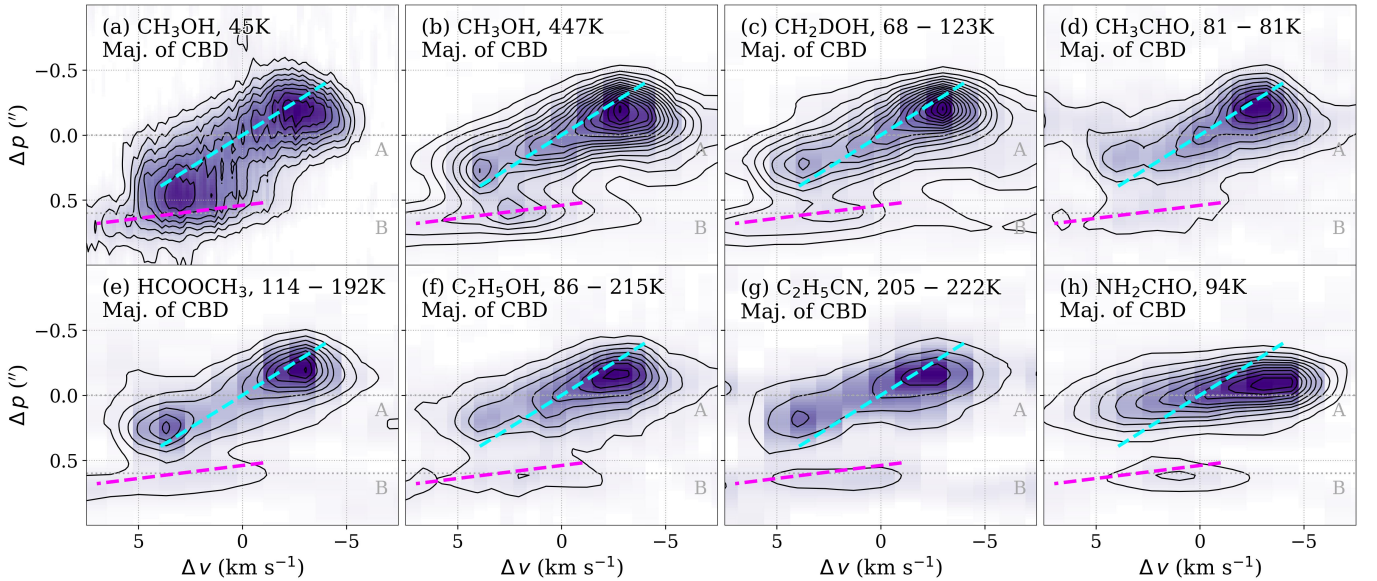


Figure 9. The PV diagrams cut along the major axis of the circumbinary disk of selected COM transitions. The reference velocity is set to 5 km s $^{-1}$. The reference position is fixed at the location of source A, while source B appears at $\Delta p = 0.^{\prime\prime}6$, as illustrated by the grey dotted lines. Contours start at 5σ and increase in steps of 5σ . Cyan and magenta dashed lines indicate the best-fit velocity structures for source A and source B, respectively, obtained from the CH₃OH PV diagrams of the two sources with the methods described in Section 4.2.

that less extended (0.^{\prime\prime}2 in Figure 8(h)) along the major axis of source A=. See Section 6.4 for further discussion of the distribution and formation of this species.

Finally, we noticed that, in Figure 9(e), the redshifted portion of the disk is relatively prominent in HCOOCH₃. This is consistent with its morphology, as shown in

Table 3. Evaluated excitation temperatures and total column densities.

Species	N_{tot}^A (cm^{-2})	N_{tot}^B (cm^{-2})	T_{ex}^A (K)	T_{ex}^B (K)
DCN;v=0;	$3.6^{+0.5}_{-0.4} \times 10^{15}$	$9.7^{+0.8}_{-1.1} \times 10^{14}$	200 [†]	200 [†]
H ₂ S;v=0;	$8.3^{+1.3}_{-1.5} \times 10^{16}$	$3.2^{+0.4}_{-0.2} \times 10^{16}$	200 [†]	200 [†]
OCS;v=0;	$5.3^{+1.1}_{-1.1} \times 10^{16}$	$3.0^{+0.3}_{-0.3} \times 10^{16}$	203^{+18}_{-10}	87^{+11}_{-9}
H ₂ CO;v=0;	$2.0^{+0.4}_{-0.5} \times 10^{17}$	$1.2^{+0.1}_{-0.1} \times 10^{17}$	187^{+10}_{-10}	326^{+11}_{-11}
D ₂ CO;v=0;	$4.2^{+0.3}_{-0.3} \times 10^{16}$	$9.9^{+0.9}_{-1.3} \times 10^{15}$	311^{+12}_{-9}	333^{+11}_{-11}
HNCO;v=0;	$6.1^{+0.7}_{-0.4} \times 10^{16}$	$7.5^{+1.5}_{-0.9} \times 10^{15}$	336^{+12}_{-11}	300^{+10}_{-15}
HCCCN;v=0;	$1.5^{+0.2}_{-0.1} \times 10^{15}$	$3.3^{+0.5}_{-0.6} \times 10^{14}$	200 [†]	200 [†]
CH ₃ OH;v=0;	$2.3^{+0.4}_{-0.3} \times 10^{18}$	$8.4^{+0.4}_{-0.3} \times 10^{17}$	218^{+11}_{-9}	227^{+8}_{-7}
CH ₃ OH;v12=1;	$2.7^{+0.7}_{-0.4} \times 10^{18}$	$5.5^{+0.9}_{-0.5} \times 10^{17}$	264^{+9}_{-7}	200 [†]
¹³ CH ₃ OH;v=0;	$2.9^{+0.6}_{-0.4} \times 10^{17}$	$6.0^{+1.7}_{-0.8} \times 10^{16}$	205^{+8}_{-8}	178^{+18}_{-10}
CH ₂ DOH;v=0;	$1.0^{+0.2}_{-0.1} \times 10^{18}$	$1.0^{+0.3}_{-0.1} \times 10^{17}$	119^{+6}_{-8}	122^{+10}_{-16}
¹³ CH ₃ CN;v=0;	$2.3^{+0.3}_{-0.2} \times 10^{15}$	$6.1^{+1.1}_{-1.1} \times 10^{14}$	297^{+12}_{-10}	309^{+9}_{-10}
CH ₃ CHO;v=0;	$1.2^{+0.1}_{-0.1} \times 10^{17}$	$2.1^{+0.2}_{-0.2} \times 10^{16}$	214^{+10}_{-7}	296^{+11}_{-17}
CH ₃ CHO;v15=1;	$1.3^{+0.1}_{-0.1} \times 10^{17}$...	252^{+8}_{-8}	...
NH ₂ CHO;v=0;	$2.2^{+0.4}_{-0.3} \times 10^{16}$	$3.3^{+0.7}_{-0.3} \times 10^{15}$	261^{+14}_{-12}	317^{+9}_{-13}
CH ₂ (OH)CHO;v=0;	$6.4^{+0.6}_{-0.6} \times 10^{16}$...	284^{+12}_{-10}	...
HCOOCH ₃ ;v=0;	$5.1^{+0.4}_{-0.4} \times 10^{17}$	$6.3^{+1.0}_{-0.5} \times 10^{16}$	291^{+11}_{-11}	262^{+17}_{-14}
HCOOCH ₃ ;v18=1;	$6.6^{+0.5}_{-0.3} \times 10^{17}$	$1.3^{+0.1}_{-0.2} \times 10^{17}$	326^{+8}_{-6}	263^{+14}_{-9}
C ₂ H ₅ OH;v=0;	$4.3^{+0.4}_{-0.4} \times 10^{17}$	$1.2^{+0.1}_{-0.2} \times 10^{17}$	335^{+12}_{-12}	306^{+12}_{-14}
C ₂ H ₅ CN;v=0;	$1.7^{+0.1}_{-0.1} \times 10^{16}$...	320^{+10}_{-8}	...
CH ₃ COCH ₃ ;v=0;	$7.7^{+1.3}_{-0.8} \times 10^{17}$...	305^{+6}_{-14}	...

NOTE—[†]The temperature is assumed to be 200 K in the simulations.

Figure 8(e), that the southeastern edge of source A is locally enhanced.

5. CHEMICAL COMPOSITIONS OF THE HOT CORINOS

5.1. Molecular Spectrum Synthesization

We further examined the molecular compositions, particularly the COMs, in the two sources using the wide-bandwidth data from project #2018.1.00302.S. At the angular resolution of these data (0''.37), the COM emission shows compact, core-like morphologies, with slight variations in peak positions among species. To minimize mutual contamination between the two sources, given the comparable beam size (0''.37) and their close separation (0''.5), we extracted spectra at the dust continuum peaks of each source. As shown in Figure 10, the two spectra shows a clear velocity offset, justifying that the emission from the two sources are well-separated. Both spectra show a forest of lines, while source A is apparently line-richer than source B. As labeled in the figure, lots of lines are the transitions of COMs, including CH₃OH, CH₃CHO, HCOOCH₃, and NH₂CHO, indicating that both source A and source B are rich in complex organic chemistry. Since line intensity depends on the gas density in each source, we need to derive

the relative column densities in order to compare the COM abundances between the two sources.

We used XCLASS (eXtended CASA Line Analysis Software Suite; Möller et al. 2017) to evaluate the excitation temperature and total column density for each molecular species. XCLASS calculates the synthetic spectra of molecular species under the assumption of local thermodynamic equilibrium (LTE), given molecular parameter inputs such as source size, excitation temperature (T_{ex}), total column density (N_{tot}), line width (δv), and velocity offset (v_{off}). To reduce degeneracy in the parameter fitting, we fixed the source size to 0''.37, the line width FWHM to 5 km s⁻¹, and the velocity offsets to 2.0 and 6.5 km s⁻¹ for source A and source B, respectively. Both the line width FWHM and the velocity offsets were estimated based on the bright CH₃OH lines, which were further examined by the synthesized spectra. For reference, the wide-bandwidth data (#2018.1.00302.S) have a spectral resolution of 1.4 km s⁻¹. The derivation of excitation temperature (T_{ex}) and total column density (N_{tot}) was performed in three steps.

1. Initial Estimation. We fixed the T_{ex} to 200 K and manually adjusted the N_{tot} to obtain a rough match with the observed line strengths.
2. Independent Fitting per Species. For each molecular species, we independently optimized T_{ex} and N_{tot} using the “Nested Sampling (NS)” algorithm. The T_{ex} was allowed to vary between 100 and 300 K. The N_{tot} was allowed to vary between 0.01 and 100 times the initial value obtained in Step 1.
3. Simultaneous Multi-Species Fitting. All molecular species were then fitted simultaneously using the NS algorithm. The T_{ex} was allowed to vary within ± 50 K of the values derived in Step 2. The N_{tot} were allowed to vary between 0.1 and 10 times the corresponding Step 2 values.
4. Error Estimation. Finally, we estimated the uncertainties of the values derived from Step 3 using the “Markov chain Monte Carlo (MCMC)” method.

Table 3 summarizes the resulting excitation temperature T_{ex} and total column density N_{tot} of each molecular species in the two sources. Figures A1-A4 in appendix show the observed and the synthesized spectra for both sources. Table A2 in appendix lists the transition parameters. We note that in source A, the COM emission extends slightly beyond the beam, meaning that our analysis captures only the bright central region. As a result, the derived column densities for source A are possibly underestimated relative to the full spatial extent of its COM emission. Particularly, CH₃OH extends beyond the beam, exhibits optical thickness in low- E_u transitions, and is additionally traced by an intervening

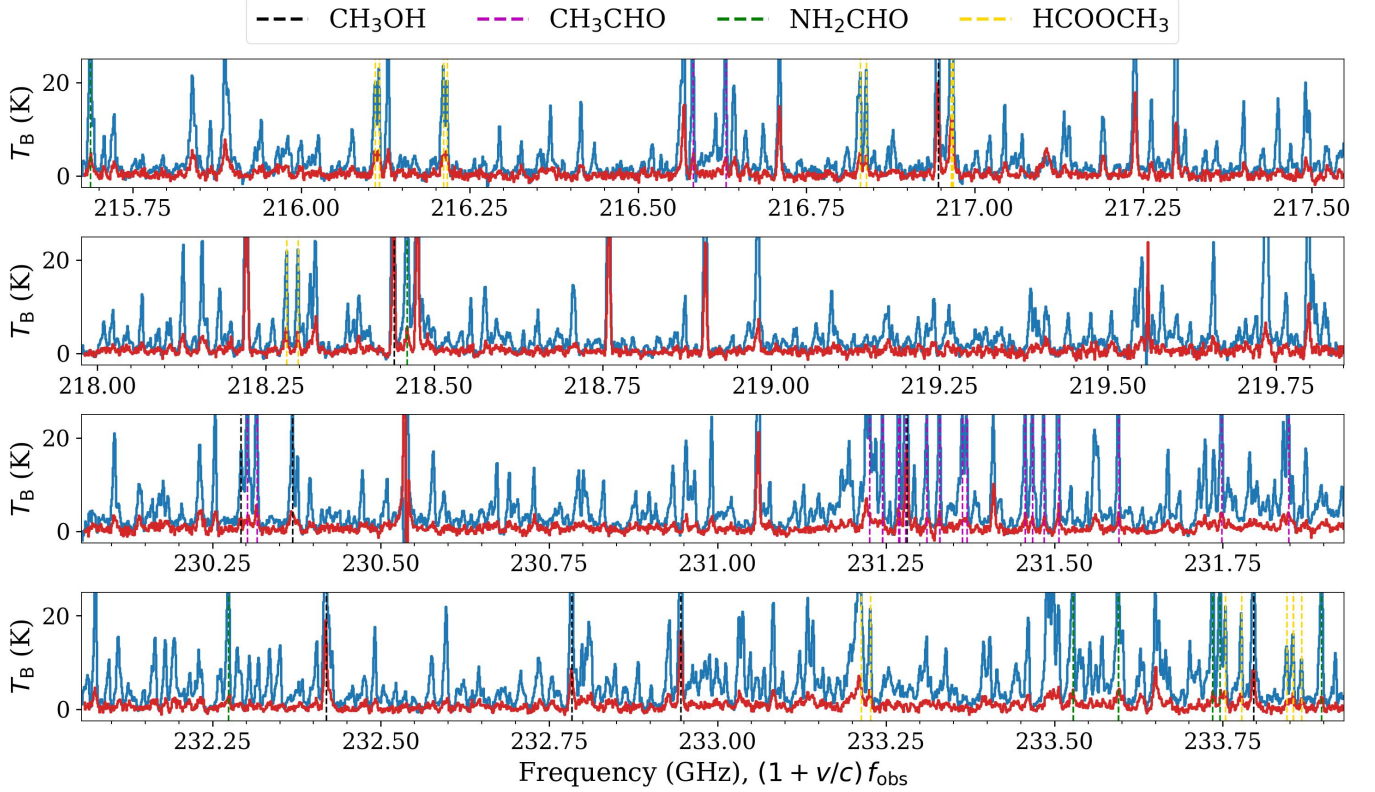


Figure 10. The spectra toward the continuum peaks of source A (blue) and B (red). The dashed lines illustrate the selected transitions of COMs. The x axis is the frequency shifted back to the expected rest frequency with $v = 2.0$ and 6.5 km s^{-1} for source A and source B, respectively.

component. Furthermore, in the future a more precise estimation could be achieved using a customized source size for each molecule, as the molecule extents are not uniform.

Among the COMs, we note that CH_3OH transitions with low upper-state energies are likely optically thick, as suggested by the images (Figure 4). In addition, high-upper-energy transitions of CH_3OH may be affected by radiative pumping in addition to collisional excitation. These effects introduce additional uncertainty into the derivation of CH_3OH column densities.

5.2. Column Densities of COMs

The $^{12}\text{C}/^{13}\text{C}$ ratios of CH_3OH , derived from the column density ratio between $\text{CH}_3\text{OH} v = 0$ and $^{13}\text{CH}_3\text{OH}$, are 8 and 13 for source A and source B, respectively. These ratios are significantly lower than the local ISM value of $\sim 50\text{--}70$ and are often interpreted as evidence that the $\text{CH}_3\text{OH} v = 0$ emission is optically thick (e.g., Zapata et al. 2013; Lee et al. 2019a; Hsu et al. 2022). The D/H ratios of CH_3OH , derived from the column density ratio between CH_2DOH and $\text{CH}_3\text{OH} v = 0$ are 0.4 and 0.1 for source A and source B, respectively. Adopting the column density of $^{13}\text{CH}_3\text{OH}$ with a $^{12}\text{C}/^{13}\text{C}$ ratio of 68 (Milam et al. 2005), the D/H ratios become 0.05 and 0.02 for source A and source B,

respectively. We note that it remains uncertain whether the low $^{12}\text{C}/^{13}\text{C}$ ratios found in hot corinos result (solely) from optically thick $\text{CH}_3\text{OH} v = 0$ emission. See Sect. 6.3 for more discussion.

In Figure 11(a), we show the column density distributions of COMs for source A and source B based on their ground vibration state transitions. Each marker represents a COM species and the two lines indicate the proportional correlations with factors of 1 and 0.1. Note that the main isotopologue of methanol, CH_3OH , is excluded, due to significant contributions from the intervening component. As shown in Figure 11(a), the column densities of source A and source B exhibit a linear pattern, indicating a comparable COM column density ratio ~ 0.1 between the two sources. This fixed ratio suggests that the COM composition in source A and source B hot corinos is similar. The higher COM column densities in source A can be attributed to its higher gas density relative to source B. For a given fractional abundance, the total number of COM molecules scales positively with gas density. Consistently, all COM lines detected in source B are also detected in source A. The COM lines detected only in source A may simply remain undetected in source B due to the lower SNR. The only line

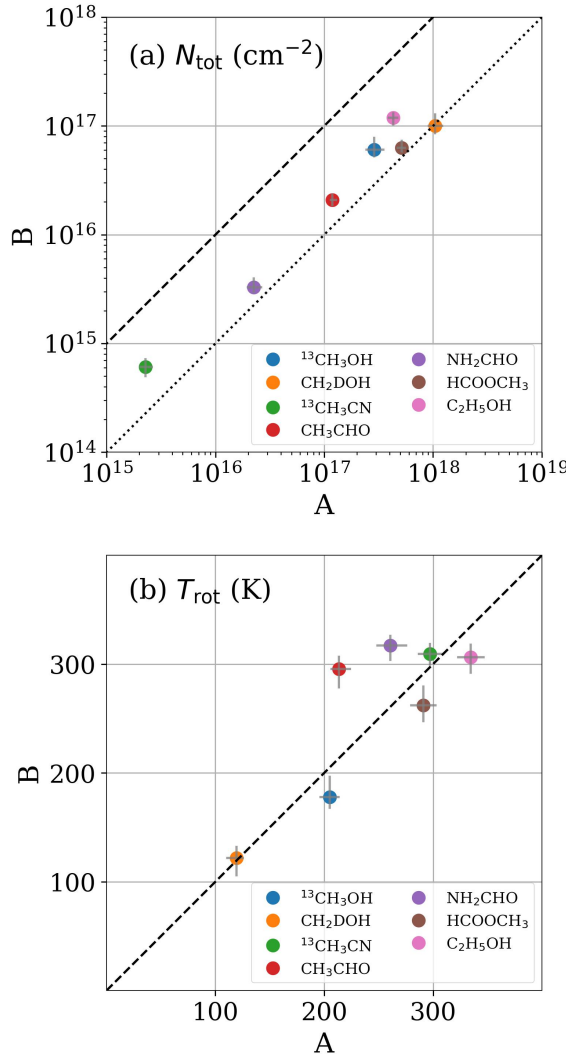


Figure 11. The column densities (a) and rotational temperature (b) distributions of selected COMs in source A and source B. In panel (a), the dashed and dotted lines illustrate the relations of $y = x$ and $y = 0.1x$, respectively. In panel (b), the dashed line illustrate the relations of $y = x$.

that is stronger in source B than source A is SiO (~ 217.1 GHz in Figure 10), which is not a COM.

5.3. Rotational Temperatures of COMs

In Figure 11(b), we show the rotational temperature distributions of COMs for source A and source B based on their ground vibration state transitions. The COMs have warm temperatures of around 100–350 K, consistent with the characteristic of a hot corino. In general, the rotational temperatures in source A are comparable to those in source B, suggesting that the COMs in the two hot corinos reside in similar thermal conditions. Meanwhile, the distributions can be tentatively divided into three groups. CH_2DOH has the lowest temperature of ~ 100 K, $^{13}\text{CH}_3\text{OH}$ and CH_3CHO

have the intermediate temperature of ~ 200 K, and the others have the highest temperature of ~ 300 K. This thermally onion-like distribution could potentially infer their different extents. For example, NH_2CHO was reported to be found to reside in more compact regions (Manigand et al. 2020; Bianchi et al. 2022; Lee et al. 2022; Okuda et al. 2022; Frediani et al. 2025).

6. DISCUSSION

6.1. Origins of the COM-rich Features in HOPS-288

Our findings suggest three COM-rich features in HOPS-288: a localized warm region in source A, a localized warm region in source B, and a feature between source A and source B (intervening CH_3OH -rich feature).

6.1.1. Hot Corino in source A

The COM emission from source A likely traces the hot inner disk, though higher resolution observations are still necessary for further confirmation. Such COM-rich features associated with disks in Class 0/I protostellar cores are rarely reported, with only a few known cases such as HH212 (Class 0; Codella et al. 2016; Lee et al. 2017, 2019a, 2022) and V883 Ori (Class I/II; van 't Hoff et al. 2018; Lee et al. 2019b; Jeong et al. 2025; Fadul et al. 2025). Detecting COM gas in disks is challenging because the warm region is extremely compact, and the dusty disk blocks irradiation from the central protostar, preventing most of the outer disk from heating (Nazari et al. 2022; Hsu et al. 2023). For HH 212, the warm disk has been attributed to direct heating from the central protostar or to interactions with disk winds (Lee et al. 2022). For V883 Ori, the presence of a warm inner disk is thought to result from a stellar outburst (van 't Hoff et al. 2018; Lee et al. 2019b; Jeong et al. 2025).

Given that the modeled stellar mass of source A suggests it is an intermediate-mass protostar as well as the observed high bolometric luminosity ($180 \pm 70 L_{\odot}$, Dutta et al. 2020; Hsu et al. 2022), we expect that the irradiation from the central protostar predominantly heats the disk. Meanwhile, the possible additional heating source includes the streamer shock from the circumbinary disk to the circumstellar disk (Tang et al. 2014) and viscous dissipation within the circumstellar disk (Liu et al. 2021). Furthermore, the binarity of source A itself could possibly bring more complication, as the COM emission can possibly be originated from a circumbinary disk.

On the other hand, the binarity of source A may also be relevant to the asymmetric morphology of COM emission in source A (Figure 4 and Figure 8). In source A, as shown in Figure 48 of Tobin et al. (2020), the northwestern substructure is the primary component in the source A, consistent with the asymmetric COM morphology of this study.

6.1.2. Hot corino in source B

Due to the limited spatial resolution, we are not able to resolve the structure of the hot corino in source B, while its rotation motion is suggested by a tentative velocity gradient. Such rotating feature can possibly be an unresolved disk or a ring (e.g., Hsu et al. 2025). The rotating ring can be attributed to the accretion shocks when materials enter the disk. Observations of COMs in other systems seem to trace the accretion shocks include L1157 Velusamy et al. (2002), IRAS 16293–2422 A Oya et al. (2016), B335 (Okuda et al. 2022), and G192.12-11.10 (Hsu et al. 2025). On another note, the shock heating on the surface of a pseudodisk is also speculated to release COMs (Wang et al. 2025).

6.1.3. CH_3OH -rich feature between source A and source B

In addition to the two hot corinos, we identify a CH_3OH -rich feature, most prominently traced in low-excitation transitions and with tentative CH_3CHO emission. This intervening component is located between source A and source B, appearing to connect source A to source B, with its peak closer to the latter. The structure may trace a shocked region within the circumbinary disk. Alternatively, it could represent a bridge linking the two sources, if the observed tail-like morphology is not a consequence of beam convolution.

The association of CH_3OH with streamer-induced shocks onto circumbinary disks has been reported in the proto-binary system [BHB2007] 11, where Vastel et al. (2022) identified three distinct CH_3OH components with different positions and velocities. They proposed that one arises from a localized region around one source, while the other two reside in the circumbinary disk and are associated with shocks driven by mass-accretion streamers. However, they also noted that alternative explanations could not be excluded, partly due to the limited spatial resolution. In our target, both the morphology and kinematics of this tail are clearly observed. The velocities and spatial extent of CH_3OH are consistent with the inner redshifted portion of the circumbinary disk (Figure 7).

A bridge has been observed in the proto-binary system IRAS 16293–2422 between the two members having a separation of 620 au (e.g., Pineda et al. 2012; van der Wiel et al. 2019). In that source, the bridge is traced by dust continuum and relatively simple molecules such as C^{17}O , C^{18}O , H_2CO , and H^{13}CN (Pineda et al. 2012; van der Wiel et al. 2019), whereas COMs, including CH_3OH , appear only at the two continuum peaks rather than along the bridge (e.g., Jørgensen et al. 2016). Furthermore, the bridge was found to be kinematically quiescent (van der Wiel et al. 2019). In contrast, in our target HOPS-288, the tail is not detected in dust continuum but is instead traced by CH_3OH . Also, the separation is around 200 au, much closer than that in IRAS

16293–2422. It is uncertain, however, as to how a quiescent bridge could lead to the desorption of CH_3OH . Therefore, the quiescent bridge scenario seen in IRAS 16293–2422 does not match HOPS-288. Regarding the scenario in which CH_3OH in HOPS-288 traces a dynamically active bridge, the enhancement of CH_3OH closer to source B could indicate a shock where material is flowing from source A toward source B. Given that source A is more massive than source B (Sect. 4.2), this would imply that the primary (more-massive) member is “feeding” the secondary (less-massive) one.

6.2. Chemical Similarities among Proto-binary/multiple Systems

6.2.1. Hot corinos exhibiting rotation motion in the Orion

As shown in Figure 11 and described in Sect. 5.2, source A and source B appear to have similar chemical compositions. In Figure 12, we present the column density ratios of source B relative to source A for the commonly detected COMs. Each bar represents the column density ratio for an individual species. As shown in Figure 12, these ratios cluster around a value of ~ 0.1 – 0.2 . We note that the column densities were derived assuming a fixed molecular source size for both source A and source B. Consequently, any difference in the actual spatial extents of the two hot corinos would introduce an additional factor (i.e., the ratio of their beam dilution) into the derived column density ratios. For example, as source A is expected to have a larger hot corino than source B, the column density ratios could be underestimated.

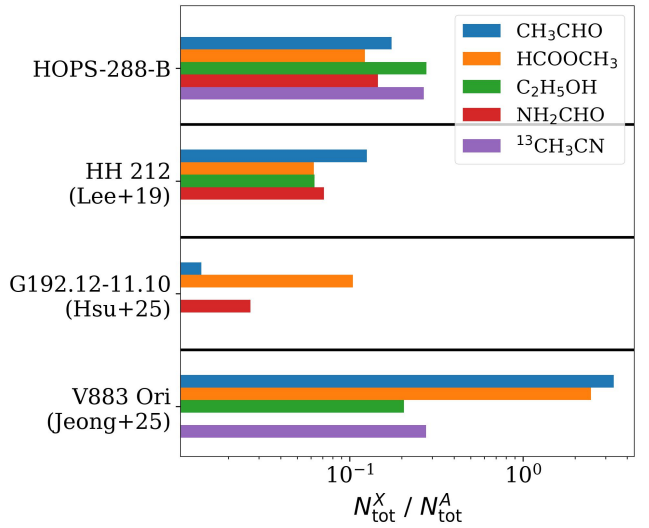


Figure 12. Column density ratios of different disk-origin hot corinos in Class 0/I protostellar cores and HOPS-288-A (source A). The protostellar core names are labeled in y-axis. Each color represents a molecular species. Comparing the relative ratios within each group provides useful insights into the chemical similarities between the labeled sources and HOPS-288-A (source A).

To further examine the observed chemical similarity between source A and source B, we compare the COM column densities between source A and those of other hot corinos in Orion that are known to exhibit rotation motions or be disk-origin: HH 212 (Lee et al. 2017, 2019a), G192.12-11.10 (Hsu et al. 2022; Hsu et al. 2025), and V883 Ori (van ’t Hoff et al. 2018; Lee et al. 2019b; Jeong et al. 2025; Fadul et al. 2025). We adopt column densities from Lee et al. (2019a) for HH 212, Hsu et al. (2022) for G192.12-11.10, and Jeong et al. (2025) for V883 Ori. Comparing the relative column density ratios between different sources provides useful insights on chemical similarity, though variations in observed transitions and analysis methodologies introduce some uncertainty. The methods used to derive the column densities in each study are summarized in Table 4. In Hsu et al. (2022), spectra were extracted at the dust continuum peak using a beam that encloses the COM emission, while in the other studies, extraction regions were chosen to adequately encompass the emitting areas (for HH 212, only the lower disk atmosphere was used).

As shown in Figure 12, in the disk of the Class 0 protostellar core HH 212, CH₃CHO is significantly more abundant than the other O-bearing (HCOOCH₃) and N-bearing (NH₂CHO) COMs. In the disk of the Class I/II protostellar core V883 Ori, CH₃CHO and HCOOCH₃ are enhanced relative to C₂H₅OH, and ¹³CH₃CN. In contrast, the column density ratios of COMs between source B and source A are very close (around 0.2), supporting the chemical similarities among proto-binary or multiple systems.

6.2.2. Chemical Similarities and Diversities among Proto-binary/multiple Systems

To our knowledge, such detailed comparisons of complex organics in proto-binary or multiple systems remain rare. In several systems, including L1551 IRS5 (50 au; Bianchi et al. 2020), L1448 IRS3B (200 au; Yang et al. 2021), Ser-emb 11 (888 au; Martín-Doménech et al. 2021), and [BHB2007] 11 (Vastel et al. 2022), hot corinos are detected in only one member. Non-detections typically result from low envelope gas densities or low luminosities, and may also be influenced by factors such as dust opacity (Sahu et al. 2019; Hsu et al. 2023). In NGC 1333 IRAS 4A (470 au), both members host COMs, but measurements toward one member are challenging due to dust opacity (López-Sepulcre et al. 2017; Sahu et al. 2019; De Simone et al. 2020). In IRAS 16293–2422, Manigand et al. (2020) compared column density ratios between sources A and B and did not find overall similarities. Given the relatively wide separation of \sim 620 au, it remains unclear how chemically similar such systems can inherit from their parental cloud.

One suitable comparison object for HOPS-288 is SVS 13A, where the two members are separated by only \sim 90 au and COMs have been detected toward both VLA4A and

VLA4B (e.g., Bianchi et al. 2019; Yang et al. 2021; Bianchi et al. 2022; Hsieh et al. 2025). Bianchi et al. (2022) reported COM abundances for VLA4A and VLA4B individually, adopting fixed rotational temperatures for each member and evaluating column densities for CH₃CHO (two lines), NH₂CHO (three lines), and CH₃OCH₃ (16 lines). The resulting column density ratios of CH₃CHO, NH₂CHO, and CH₃OCH₃ between the two members were 0.46, 0.24, and 1.33, respectively. As pointed out by Bianchi et al. (2022), their observed chemical segregation between the two members may result from the onion-like structure of the two hot corinos. For example, compared to the other COMs, NH₂CHO is formed in a compact region and consequently be more easily obscured by the dust. Therefore, its column density in the member having more optically thick dust continuum (VLA4B) could be more underestimated than the other one (VLA4A). Given the limited number of proto-binary/multiple systems studied in detail, the question of how chemical compositions compare between members within proto-binary/multiple systems remains largely open.

6.2.3. Implications

Here we propose three scenarios to interpret the chemical similarities in COMs between the YSOs within the close binary/multiple system HOPS-288: (i) early chemical imprint, (ii) common reservoir accretion, and (iii) inter-source exchange. First, if source A and source B are evolving independently, the observed similarity would suggest that the chemical composition is established even earlier, possibly during the starless core phase. Considering that source A may be at a more evolved stage than source B (Section 3.2), the observed chemical similarity between them may further indicate that the chemistry of commonly detected COMs does not change substantially with protostellar evolution at these early stages. Second, the similarities may reflect a common chemical reservoir, where material is funneled toward the two hot corinos. The reservoir could be either the circumbinary disk or gas components at an even larger scale. The role of streamers in shaping COM chemistry has been suggested, for example, to explain the unusual ¹²C/¹³C ratio of methyl cyanide in SVS 13A (Hsieh et al. 2025), despite the other scenarios were also proposed (Busch et al. 2025). If streamers can indeed significantly influence the COM composition of the accreting protostellar core, then the observed COM similarity would imply that the streamers themselves share chemically similar, or even identical, origins. Finally, the similarities may arise from material exchange between the two members. In this scenario, comparable chemical compositions would be naturally expected, as one member accretes material from the other. The intervening component identified in this study between source A and source B could potentially trace such

Table 4. The information of the studies of hot corinos in the Orion cloud and exhibiting rotation motion or disk-originated.

Reference	Source	Method	Fixed Parameters
This study	HOPS-288	Spectrum Fitting	$\delta v = 5 \text{ km s}^{-1}$
Lee et al. (2019a)	HH 212	Rotational Diagram (Optically thin)	$T_{\text{rot}} = 150 \text{ K}$
Hsu et al. (2022)	G192.12-11.10	Spectrum Fitting	
Jeong et al. (2025)	V883 Ori	Spectrum Fitting	$T_{\text{rot}} = 120 \text{ K}; \delta v = 3 \text{ km s}^{-1}$

interactions, serving as a bridge for the transfer of material between the two sources.

The three proposed scenarios are not mutually exclusive. Namely, the two sources could inherit similar materials from their parent cloud, absorb the materials from a coherent nearby reservoir, and then exchange material with each other.

6.2.4. *Caveats*

The reported chemical similarities are based on the derived column densities, which could be affected by several factors.

Although we often refer to the warm region rich in COMs surrounding a solar-type protostar as a hot corino, the spatial distributions of individual COMs within this region may differ (e.g., Bianchi et al. 2022; Hsu et al. 2024). In reality, different COM species can have distinct emitting extents, line widths, and even velocity centroids. However, in our analysis, these parameters were fixed, which could introduce uncertainties in the derived column densities. For example, a component size of $\sim 0''.2$ (the deconvolved continuum size of source B) could possibly lead to an underestimation of column densities by a factor of two. Meanwhile, we do not account for the potential effect of dust opacity, which could lead to underestimated molecular column densities. A well-known example is NGC 1333 IRAS 4A1, where Sahu et al. (2019) detected COM absorption lines at millimeter wavelengths and proposed that dust opacity was responsible. Subsequently, De Simone et al. (2020) revealed COM emission from the same source at centimeter wavelengths, further supporting the influence of dust opacity. Our target, HOPS-288, is likely a nearly edge-on system and therefore could also be affected by dust opacity. A similar situation is seen in the nearly edge-on disk of HH 212, where COM emission exhibits a “hamburger-like” morphology due to the midplane being thermalized by optically thick dust (Lee et al. 2017, 2019a, 2022). Detecting gas-phase COMs in disks is additionally difficult due to the small warm region (e.g., Nazari et al. 2022; Hsu et al. 2023). As a result, the detected COMs associated with disks are often at the periphery of the disk, such as the surface atmosphere in HH 212 and the disk-envelope interface (e.g., Oya et al. 2016; Okoda et al. 2022; Hsu et al. 2025). Similarly, Bianchi et al. (2022) suggested that the observed chemical segregation in SVS 13A may be

linked to the layered spatial extents of COMs, as well as to dust opacity effects. In our observations, the hot corinos are not spatially well resolved and we cannot rule out the role of the dust opacity.

6.3. $^{12}\text{C}/^{13}\text{C}$ ratio of CH_3OH

As shown in Sect. 5.2, the $^{12}\text{C}/^{13}\text{C}$ ratios of CH_3OH are 12 and 8 for source A and source B, respectively, indicating that $\text{CH}_3\text{OH} v = 0$ emission is optically thick. However, similarly low $^{12}\text{C}/^{13}\text{C}$ ratios of CH_3OH are commonly observed in hot corinos (e.g., Hsu et al. 2022; Busch et al. 2025). Moreover, (Lee et al. 2023) reported that even ratios derived from optically thin transitions of $\text{CH}_3\text{OH} v = 2$ remain as low as about 20. This raises the question of whether the generally low $^{12}\text{C}/^{13}\text{C}$ ratios result (solely) from optically thick $\text{CH}_3\text{OH} v = 0$ emission. To address this, Busch et al. (2025) suggests that ^{13}C enrichment in COMs during early protostellar stages can be inherited from precursor species. The $^{12}\text{C}/^{13}\text{C}$ ratios in the prestellar phase are established through isotopic exchange reactions. More studies are necessary for further confirmations.

6.4. *Implications of Formamide*

NH_2CHO is suggested as a pre-biotic precursor (e.g., Saladino et al. 2012; López-Sepulcre et al. 2019). In Figures 8 and 9, NH_2CHO is found to reside in much more compact regions than the other COMs. Similar behavior has been reported in, for example, IRAS 16293-2422 A (Manigand et al. 2020) and HH 212 (Lee et al. 2022). Lee et al. (2022) showed that the extents of NH_2CHO , CH_3OH , and H_2CO are anti-correlated with their binding energies, consistent with these molecules being thermally desorbed from icy mantles in the disk. Beyond the thermal desorption of NH_2CHO from dust-grain mantles, its compact morphology in HOPS-288 may also suggest that NH_2CHO formation on ices is enhanced in the warmer, inner regions. This could be related to external vacuum-ultraviolet (VUV) irradiation, as laboratory experiments by Martín-Doménech et al. (2020) demonstrated that NH_2CHO formation from radicals can be significantly boosted under VUV irradiation. On the other hand, López-Sepulcre et al. (2024) demonstrated that the NH_2CHO observed in the

outflow L1157-B can be largely explained by gas-phase chemistry, specifically via the reaction $\text{H}_2\text{CO} + \text{NH}_2 \rightarrow \text{NH}_2\text{CHO} + \text{H}_2$. However, since their modeling was tailored to the outflow environment (e.g., molecular hydrogen number density of $4 \times 10^5 \text{ cm}^{-3}$), the same conclusion may not be directly applicable to disk environments such as the hot corinos in HH 212 and HOPS-288.

7. CONCLUSIONS

Utilizing two ALMA programs, #2018.1.01038.S and #2018.1.00302.S, we investigated the physical structure as well as the morphology, kinematics, and compositions of COMs in the hierarchical 2+1 proto-triple system HOPS-288. The system was treated as a proto-binary, consisting of HOPS-288-A and HOPS-288-B, since the local binarity of the former can not be resolved.

1. We identified two CO outflows, each associated with one source, along with a C^{18}O circumbinary disk.
2. We revealed three COM-rich features in HOPS-288: two hot corinos associated with HOPS-288-A and HOPS-288-B, and an intervening component between them. The intervening component is traced by CH_3OH (particularly its low- E_u transitions) and tentatively by CH_3CHO , whereas the other COMs appear confined to the two hot corinos. Both the hot corinos in HOPS-288-A and HOPS-288-B are likely tracing rotation motions. The kinematics of the former further suggests its disk origin. The latter is indicated by a tentative velocity gradient along its major axis. An intervening component may trace a shocked region within the circumbinary disk induced by a mass accretion streamer. Alternatively, if the tail-like morphology is not resulting from beam convolution, this component could primarily represent a bridge linking the two sources.
3. We derived the rotational temperatures and column densities of molecules in the inner part of HOPS-288-A and HOPS-288-B. The derived column density ratios of COMs are similar between the two sources, suggesting comparable complex organic chemistry. Additional uncertainties could be possibly caused by dust opacity and the diverse COM extents. We propose three possible scenarios to explain these similarities: (i) inter-source exchange, (ii) common reservoir accretion, and (iii) early chemical imprint.
4. The $^{12}\text{C}/^{13}\text{C}$ ratios of CH_3OH , derived from the column density ratios of $\text{CH}_3\text{OH} v = 0$ to $^{13}\text{CH}_3\text{OH}$, are ~ 10 , significantly below the interstellar medium value of $\sim 50\text{--}70$. The D/H ratios of CH_3OH , calculated from the column density ratios of CH_2DOH

to $\text{CH}_3\text{OH} v = 0$, are 0.4 and 0.1 for sources A and B, respectively. Assuming a $^{12}\text{C}/^{13}\text{C}$ ratio of 68 and using the $^{13}\text{CH}_3\text{OH}$ column density, the adjusted D/H ratios are 0.05 and 0.02 for sources A and B, respectively. Low $^{12}\text{C}/^{13}\text{C}$ ratios in CH_3OH are commonly observed in hot corinos, but it remains unclear whether these low values result solely from optically thick emission in $\text{CH}_3\text{OH} v = 0$.

5. Within the hot corino in HOPS-288-A, the COM emission shows an asymmetric brightness distribution: the blueshifted side is systematically brighter than the redshifted side. Such effect is less pronounced in HCOOCH_3 . In addition, NH_2CHO emission is concentrated in more compact, inner regions compared to other COMs

ACKNOWLEDGMENTS

This paper makes use of the following ALMA data: ADS/JAO.ALMA#2018.1.00302.S and ADS/JAO.ALMA#2018.1.01038.S. ALMA is a partnership of ESO (representing its member states), NSF (USA) and NINS (Japan), together with NRC (Canada), NSTC and ASIAA (Taiwan), and KASI (Republic of Korea), in cooperation with the Republic of Chile. The Joint ALMA Observatory is operated by ESO, AUI/NRAO and NAOJ. This work made use of Astropy:¹ a community-developed core Python package and an ecosystem of tools and resources for astronomy (Astropy Collaboration et al. 2013; Price-Whelan et al. 2018; Astropy Collaboration et al. 2022). S.-Y.H. acknowledges support from the Academia Sinica of Taiwan (grant No. AS-PD-1142-M02-2). S.-Y. H. and C.-F.L. acknowledge grant from the National Science and Technology Council of Taiwan (112-2112-M-001- 039-MY3). N.M.M. acknowledges support from the DGAPA-PAPIIT IA103025 grant. D.J. is supported by NRC Canada and by an NSERC Discovery Grant. Supported by the international Gemini Observatory, a program of NSF's NOIRLab, which is managed by the Association of Universities for Research in Astronomy (AURA) under a cooperative agreement with the National Science Foundation, on behalf of the Gemini partnership of Argentina, Brazil, Canada, Chile, the Republic of Korea, and the United States of America. L. B. gratefully acknowledges support by the ANID BASAL project FB210003. Q-Y.L acknowledges the support by JSPS KAKENHI Grant Number JP23K20035.

Software: Astropy (Astropy Collaboration et al. 2013; Price-Whelan et al. 2018; Astropy Collaboration et al. 2022), CASA (CASA Team et al. 2022), CARTA (Comrie et al. 2021), XCLASS (Möller et al. 2017).

APPENDIX

Table A1. Transitions used in this study covered by the high-resolution (#2018.1.01038.S) data.

Species	f_{rest}	E_u	A_{ij}	g_u	Quantum Numbers
	(MHz)	(K)			(s^{-1})
CO	230538.00	17	6.9106E-07	5	v=0; 2 - 1
C^{18}O	219560.35	16	6.0116E-07	5	v=0; 2 - 1
SO	219949.44	35	1.3352E-04	13	S=1; v=0; J=6-5; N=5-4
CH_3OH	218440.05	45	4.6863E-05	36	v=0; 4 _(2,3) - 3 _(1,2) ; E
CH_3OH	232945.00	190	2.1267E-05	84	v=0; 10 _(3,7) - 11 _(2,9) ; E
CH_3OH	232783.50	447	2.1649E-05	148	v=0; 18 _(3,16) - 17 _(4,13) ; A1
CH_3OH	230368.70	683	2.0794E-05	180	v=0; 22 _(4,18) - 21 _(5,16) ; E
CH_2DOH	233133.91	68	2.3468E-06	11	v=0; 5 _(3,3) - 4 _(2,3) ; e0-e1
CH_2DOH	233083.13	68	2.3254E-06	11	v=0; 5 _(3,2) - 4 _(2,2) ; e0-e1
CH_2DOH	233461.15	123	8.6800E-06	19	v=0; 9 _(2,8) - 9 _(1,9) ; e1
CH_3CHO	230301.92	81	4.1938E-04	50	v=0; 12 _(2,11) - 11 _(2,10) ; A
CH_3CHO	230315.79	81	4.1933E-04	50	v=0; 12 _(2,11) - 11 _(2,10) ; E
HCOOCH_3	233777.52	114	1.8391E-04	74	v=0; 18 _(4,14) - 17 _(4,13) ; A
HCOOCH_3	233867.19	192	1.2860E-04	78	v=0; 19 _(11,9) - 18 _(11,8) ; E
$\text{C}_2\text{H}_5\text{OH}$	230991.38	86	1.1962E-04	29	14 _(0,14) - 13 _(1,13) ; A
$\text{C}_2\text{H}_5\text{OH}$	230672.56	139	1.0602E-04	27	13 _(2,11) - 12 _(2,10) ; G ⁺
$\text{C}_2\text{H}_5\text{OH}$	230230.74	143	8.2078E-05	27	13 _(2,11) - 12 _(2,10) ; G ⁻
$\text{C}_2\text{H}_5\text{OH}$	230953.78	146	7.7648E-05	33	16 _(5,11) - 16 _(4,12) ; A
$\text{C}_2\text{H}_5\text{OH}$	230473.01	215	1.4244E-05	37	18 _(3,11) - 17 _(4,14) ; G ⁻ - G ⁺
$\text{C}_2\text{H}_5\text{CN}$	233443.10	179	1.0368E-03	53	26 _(5,22) - 25 _(5,21)
$\text{C}_2\text{H}_5\text{CN}$	233069.31	205	9.9390E-04	53	26 _(7,20) - 25 _(7,19)
$\text{C}_2\text{H}_5\text{CN}$	233069.38	205	9.9390E-04	53	26 _(7,19) - 25 _(7,18)
$\text{C}_2\text{H}_5\text{CN}$	232998.74	222	9.6916E-04	53	26 _(8,19) - 25 _(8,18)
$\text{C}_2\text{H}_5\text{CN}$	232998.74	222	9.6916E-04	53	26 _(8,18) - 25 _(8,17)
NH_2CHO	233896.58	94	8.6203E-04	23	11 _(3,9) - 10 _(3,8)

A. MOLECULAR TRANSITIONS

Tables A1 and A2 list the molecular transitions covering by the high-resolution (#2018.1.01038.S) and wide-bandwidth (#2018.1.00302.S), respectively. Figures A1, A2, A3, and A4 show the observed spectra and the modeled spectra from XCLASS fitting.

Table A2. Transitions used in this study covered by the wide-bandwidth (#2018.1.00302.S) data.

Species	f_{rest}	E_u	A_{ij}	g_u	Quantum Numbers
	(MHz)	(K)			(s^{-1})
H_2CO	216568.65	174	7.2219E-06	57	9 _(1,8) - 9 _(1,9)
H_2CO	218760.07	68	1.5774E-04	7	3 _(2,1) - 2 _(2,0)
H_2CO	218475.63	68	1.5714E-04	7	3 _(2,2) - 2 _(2,1)
H_2CO	218222.19	21	2.8180E-04	7	3 _(0,3) - 2 _(0,2)
D_2CO	233650.44	50	2.6888E-04	18	4 _(2,3) - 3 _(2,2)
D_2CO	231410.23	28	3.4744E-04	18	4 _(0,4) - 3 _(0,3)

Table A2 *continued*

Species	f_{rest}	E_u	A_{ij}	g_u	Quantum Numbers
	(MHz)	(K)			(s^{-1})
CH_3OH	218440.05	45	4.6863E-05	36	v=0; 4 _(2,3) - 3 _(1,2) ; E
CH_3OH	216945.60	56	1.2135E-05	44	v=0; 5 _(1,4) - 4 _(2,3) ; E
CH_3OH	232418.59	165	1.8675E-05	84	v=0; 10 _(2,8) - 9 _(3,7) ; A1
CH_3OH	231281.10	165	1.8314E-05	84	v=0; 10 _(2,9) - 9 _(3,6) ; A2
CH_3OH	232945.00	190	2.1267E-05	84	v=0; 10 _(3,7) - 11 _(2,9) ; E
CH_3OH	233795.75	447	2.1978E-05	148	v=0; 18 _(3,15) - 17 _(4,14) ; A2
CH_3OH	232783.50	447	2.1649E-05	148	v=0; 18 _(3,16) - 17 _(4,13) ; A1
CH_3OH	230368.70	683	2.0794E-05	180	v=0; 22 _(4,18) - 21 _(5,16) ; E
CH_3OH	233121.26	745	1.0539E-05	92	v=1; 11 _(6,5) - 11 _(7,4) ; E
CH_3OH	217299.20	374	4.2846E-05	52	v=1; 6 _(1,5) - 7 _(2,5) ; A2
$^{13}\text{CH}_3\text{OH}$	233487.92	815	2.1510E-05	49	v=0; 24 _(5,20) - 23 _(6,18) ; E2
$^{13}\text{CH}_3\text{OH}$	231818.38	594	3.8732E-05	45	v=0; 22 _(1,21) - 22 _(0,22) ; E2
$^{13}\text{CH}_3\text{OH}$	217044.62	254	2.3746E-05	29	v=0; 14 _(1,13) - 13 _(2,12) ; A2
$^{13}\text{CH}_3\text{OH}$	217399.55	162	1.5272E-05	21	v=0; 10 _(2,8) - 9 _(3,7) ; A1
$^{13}\text{CH}_3\text{OH}$	216370.39	162	1.4987E-05	21	v=0; 10 _(2,9) - 9 _(3,6) ; A2
$^{13}\text{CH}_3\text{OH}$	215886.96	45	4.5276E-05	9	v=0; 4 _(2,2) - 3 _(1,2) ; E2
CH_2DOH	219551.49	48	5.0949E-06	11	v=0; 5 _(1,5) - 4 _(1,4) ; e1
CH_2DOH	233083.13	68	2.3254E-06	11	v=0; 5 _(3,2) - 4 _(2,2) ; e0-e1
CH_2DOH	218316.39	59	6.6880E-06	11	v=0; 5 _(2,4) - 5 _(1,5) ; e1
CH_2DOH	232929.02	49	3.2564E-06	7	v=0; 3 _(3,0) - 4 _(2,3) ; e0
CH_2DOH	233461.15	123	8.6800E-06	19	v=0; 9 _(2,8) - 9 _(1,9) ; e1
CH_2DOH	231840.30	124	1.2209E-05	21	v=0; 10 _(1,9) - 9 _(2,8) ; e0
CH_2DOH	216129.63	167	1.5496E-05	25	v=0; 12 _(0,12) - 11 _(1,11) ; e0-e1
CH_2DOH	233141.75	261	2.2225E-05	29	v=0; 14 _(2,12) - 14 _(1,13) ; e1
CH_2DOH	230376.57	293	2.2760E-05	31	v=0; 15 _(2,13) - 15 _(1,14) ; e1
CH_2DOH	230254.23	310	6.5037E-05	33	v=0; 16 _(2,14) - 16 _(1,15) ; e0
CH_2DOH	233209.88	347	6.4920E-05	35	v=0; 17 _(2,15) - 17 _(1,16) ; e0
CH_2DOH	233602.96	884	2.4365E-05	57	v=0; 28 _(2,27) - 28 _(1,28) ; e0-e1
CH_2DOH	233735.66	105	2.6980E-06	15	v=0; 7 _(3,5) - 8 _(2,6) ; e1-e0
$\text{C}_2\text{H}_5\text{OH}$	218554.51	226	7.1845E-05	43	21 _(5,16) - 21 _(4,17) ; A
$\text{C}_2\text{H}_5\text{OH}$	231790.06	245	8.4615E-05	45	22 _(5,18) - 22 _(4,19) ; A
$\text{C}_2\text{H}_5\text{OH}$	232318.51	264	8.5858E-05	47	23 _(5,19) - 23 _(4,20) ; A
$\text{C}_2\text{H}_5\text{OH}$	230144.81	284	5.4589E-05	51	25 _(3,23) - 25 _(2,24) ; A
$\text{C}_2\text{H}_5\text{OH}$	233208.54	284	8.7396E-05	49	24 _(5,20) - 24 _(4,21) ; A
$\text{C}_2\text{H}_5\text{OH}$	217238.29	792	1.5185E-05	81	40 _(9,31) - 39 _(10,30) ; A
$\text{C}_2\text{H}_5\text{OH}$	217400.43	464	1.7655E-05	63	31 _(6,26) - 30 _(7,23) ; A
$\text{C}_2\text{H}_5\text{OH}$	231789.85	506	2.2387E-05	63	31 _(5,27) - 31 _(4,27) ; G ⁻ - G ⁺
$\text{C}_2\text{H}_5\text{OH}$	231840.75	685	1.0785E-05	71	35 _(9,26) - 34 _(10,24) ; G ⁻ - G ⁺
$\text{C}_2\text{H}_5\text{OH}$	232422.96	923	1.5956E-05	87	43 _(8,35) - 42 _(9,33) ; G ⁺ - G ⁻
$\text{C}_2\text{H}_5\text{OH}$	215890.45	294	6.3232E-05	51	25 _(4,22) - 25 _(3,23) ; A
$\text{C}_2\text{H}_5\text{OH}$	231558.57	226	8.3570E-05	43	21 _(5,17) - 21 _(4,18) ; A
$\text{C}_2\text{H}_5\text{OH}$	231737.62	191	8.1839E-05	39	19 _(5,15) - 19 _(4,16) ; A
$\text{C}_2\text{H}_5\text{OH}$	230793.86	105	6.2028E-05	13	6 _(5,2) - 5 _(4,2) ; G ⁺ - G ⁻
$\text{C}_2\text{H}_5\text{OH}$	230793.76	105	6.2028E-05	13	6 _(5,1) - 5 _(4,1) ; G ⁺ - G ⁻
$\text{C}_2\text{H}_5\text{OH}$	233601.55	120	7.7124E-05	29	14 _(5,10) - 14 _(4,11) ; A
$\text{C}_2\text{H}_5\text{OH}$	232928.53	120	7.6535E-05	29	14 _(5,9) - 14 _(4,10) ; A
$\text{C}_2\text{H}_5\text{OH}$	216415.67	131	9.0183E-05	27	13 _(0,13) - 12 _(0,12) ; G ⁺
$\text{C}_2\text{H}_5\text{OH}$	233215.50	132	7.8327E-05	31	15 _(5,11) - 15 _(4,12) ; A
$\text{C}_2\text{H}_5\text{OH}$	230991.38	86	1.1962E-04	29	14 _(0,14) - 13 _(1,13) ; A

Table A2 *continued*

Table A2 (continued)

Species	f_{rest}	E_u	A_{ij}	g_u	Quantum Numbers
	(MHz)	(K)	(s^{-1})		
$\text{C}_2\text{H}_5\text{OH}$	218461.23	24	6.3782E-05	11	$5_{(3,2)} - 4_{(2,3)}$; A
$\text{C}_2\text{H}_5\text{OH}$	231560.92	208	8.2653E-05	41	$20_{(5,16)} - 20_{(4,17)}$; A
$\text{C}_2\text{H}_5\text{OH}$	217496.67	135	6.8662E-05	27	$13_{(1,13)} - 12_{(0,12)}$; G ⁻
$\text{C}_2\text{H}_5\text{OH}$	232075.85	132	7.7291E-05	31	$15_{(5,10)} - 15_{(4,11)}$; A
$\text{C}_2\text{H}_5\text{OH}$	230672.56	139	1.0602E-04	27	$13_{(2,11)} - 12_{(2,10)}$; G ⁺
$\text{C}_2\text{H}_5\text{OH}$	232491.32	142	1.1210E-04	29	$14_{(0,14)} - 13_{(0,13)}$; G ⁺
$\text{C}_2\text{H}_5\text{OH}$	231668.74	142	1.1080E-04	29	$14_{(1,14)} - 13_{(1,13)}$; G ⁺
$\text{C}_2\text{H}_5\text{OH}$	230230.74	143	8.2078E-05	27	$13_{(2,11)} - 12_{(2,10)}$; G ⁻
$\text{C}_2\text{H}_5\text{OH}$	232808.86	146	7.9330E-05	33	$16_{(5,12)} - 16_{(4,13)}$; A
$\text{C}_2\text{H}_5\text{OH}$	230953.78	146	7.7648E-05	33	$16_{(5,11)} - 16_{(4,12)}$; A
$\text{C}_2\text{H}_5\text{OH}$	232596.57	147	8.0717E-05	29	$14_{(1,14)} - 13_{(1,13)}$; G ⁻
$\text{C}_2\text{H}_5\text{OH}$	232404.84	160	8.0221E-05	35	$17_{(5,13)} - 17_{(4,14)}$; A
$\text{C}_2\text{H}_5\text{OH}$	217262.30	136	6.2719E-05	27	$13_{(0,13)} - 12_{(1,12)}$; G ⁻
$\text{C}_2\text{H}_5\text{OH}$	230793.86	105	6.2028E-05	13	$6_{(5,2)} - 5_{(4,2)}$; G ⁺ - G ⁻
$\text{C}_2\text{H}_5\text{OH}$	230793.76	105	6.2028E-05	13	$6_{(5,1)} - 5_{(4,1)}$; G ⁺ - G ⁻
CH_3CHO	231484.37	108	3.8971E-04	50	v=0; $12_{(4,8)} - 11_{(4,7)}$; E
CH_3CHO	231506.29	108	3.8969E-04	50	v=0; $12_{(4,9)} - 11_{(4,8)}$; E
CH_3CHO	231748.72	93	4.0896E-04	50	v=0; $12_{(3,10)} - 11_{(3,9)}$; E
CH_3CHO	231595.27	93	4.1153E-04	50	v=0; $12_{(3,10)} - 11_{(3,9)}$; A
CH_3CHO	231225.54	183	2.8833E-04	50	v=0; $12_{(7,5)} - 11_{(7,4)}$; E
CH_3CHO	230315.79	81	4.1933E-04	50	v=0; $12_{(2,11)} - 11_{(2,10)}$; E
CH_3CHO	230301.92	81	4.1938E-04	50	v=0; $12_{(2,11)} - 11_{(2,10)}$; A
CH_3CHO	216581.93	65	3.5458E-04	46	v=0; $11_{(1,10)} - 10_{(1,9)}$; E
CH_3CHO	231847.58	93	4.0964E-04	50	v=0; $12_{(3,9)} - 11_{(3,8)}$; E
CH_3CHO	231245.03	183	2.8843E-04	50	v=0; $12_{(7,5)} - 11_{(7,4)}$; A
CH_3CHO	231245.03	183	2.8843E-04	50	v=0; $12_{(7,6)} - 11_{(7,5)}$; A
CH_3CHO	231268.39	183	2.8842E-04	50	v=0; $12_{(7,6)} - 11_{(7,5)}$; E
CH_3CHO	231269.90	153	3.2800E-04	50	v=0; $12_{(6,7)} - 11_{(6,6)}$; A
CH_3CHO	231269.90	153	3.2800E-04	50	v=0; $12_{(6,6)} - 11_{(6,5)}$; A
CH_3CHO	231278.98	153	3.2793E-04	50	v=0; $12_{(6,6)} - 11_{(6,5)}$; E
CH_3CHO	231310.50	153	3.2803E-04	50	v=0; $12_{(6,7)} - 11_{(6,6)}$; E
CH_3CHO	231456.74	108	3.8965E-04	50	v=0; $12_{(4,9)} - 11_{(4,8)}$; A
CH_3CHO	231467.50	108	3.8967E-04	50	v=0; $12_{(4,8)} - 11_{(4,7)}$; A
CH_3CHO	231369.83	129	3.6174E-04	50	v=0; $12_{(5,8)} - 11_{(5,7)}$; E
CH_3CHO	231363.28	129	3.6168E-04	50	v=0; $12_{(5,7)} - 11_{(5,6)}$; E
CH_3CHO	231329.64	129	3.6172E-04	50	v=0; $12_{(5,8)} - 11_{(5,7)}$; A
CH_3CHO	231329.79	129	3.6172E-04	50	v=0; $12_{(5,7)} - 11_{(5,6)}$; A
CH_3CHO	231245.03	183	2.8843E-04	50	v=0; $12_{(7,5)} - 11_{(7,4)}$; A
CH_3CHO	231245.03	183	2.8843E-04	50	v=0; $12_{(7,6)} - 11_{(7,5)}$; A
CH_3CHO	231269.90	153	3.2800E-04	50	v=0; $12_{(6,7)} - 11_{(6,6)}$; A
CH_3CHO	231269.90	153	3.2800E-04	50	v=0; $12_{(6,6)} - 11_{(6,5)}$; A
CH_3CHO	231235.14	216	2.4279E-04	50	v=0; $12_{(8,4)} - 11_{(8,3)}$; A
CH_3CHO	231235.14	216	2.4279E-04	50	v=0; $12_{(8,5)} - 11_{(8,4)}$; A
CH_3CHO	216969.89	556	1.0525E-05	134	v=0; $33_{(4,30)} - 32_{(5,27)}$; E
CH_3CHO	231226.97	255	1.9119E-04	50	v=0; $12_{(9,3)} - 11_{(9,2)}$; A
CH_3CHO	231226.97	255	1.9119E-04	50	v=0; $12_{(9,4)} - 11_{(9,3)}$; A
CH_3CHO	231226.97	255	1.9119E-04	50	v=0; $12_{(9,3)} - 11_{(9,2)}$; A
CH_3CHO	231226.97	255	1.9119E-04	50	v=0; $12_{(9,4)} - 11_{(9,3)}$; A
CH_3CHO	231357.35	299	4.1129E-04	50	v=1; $12_{(3,9)} - 11_{(3,8)}$; E
CH_3CHO	233048.52	285	4.3142E-04	50	v=1; $12_{(2,11)} - 11_{(2,10)}$; E
CH_3CHO	232576.45	297	4.1627E-04	50	v=1; $12_{(3,9)} - 11_{(3,8)}$; A
CH_3CHO	230395.16	286	4.2196E-04	50	v=1; $12_{(2,11)} - 11_{(2,10)}$; A
CH_3CHO	232804.10	288	4.3087E-04	50	v=1; $12_{(2,10)} - 11_{(2,9)}$; E

Table A2 (continued)

Species	f_{rest}	E_u	A_{ij}	g_u	Quantum Numbers
	(MHz)	(K)	(s^{-1})		
CH_3CHO	230144.55	290	4.8749E-05	54	v=1; $13_{(0,13)} - 12_{(1,12)}$; A
CH_3CHO	232422.03	297	4.1335E-04	50	v=1; $12_{(3,10)} - 11_{(3,9)}$; E
CH_3CHO	232165.52	297	4.1414E-04	50	v=1; $12_{(3,10)} - 11_{(3,9)}$; A
CH_3CHO	233852.03	784	5.4483E-05	138	v=1; $34_{(3,31)} - 34_{(2,32)}$; A
CH_3CHO	231927.65	763	1.0281E-05	114	v=1; $28_{(9,19)} - 29_{(8,22)}$; A
CH_3CHO	231928.14	763	1.0281E-05	114	v=1; $28_{(9,20)} - 29_{(8,21)}$; A
CH_3CHO	231874.70	457	1.9107E-04	50	v=1; $12_{(9,4)} - 11_{(9,3)}$; E
CH_3CHO	231927.65	763	1.0281E-05	114	v=1; $28_{(9,19)} - 29_{(8,22)}$; A
CH_3CHO	231928.14	763	1.0281E-05	114	v=1; $28_{(9,20)} - 29_{(8,21)}$; A
CH_3CHO	231927.47	357	3.2852E-04	50	v=1; $12_{(6,7)} - 11_{(6,6)}$; A
CH_3CHO	231927.47	357	3.2852E-04	50	v=1; $12_{(6,6)} - 11_{(6,5)}$; A
CH_3CHO	232180.10	332	3.6284E-04	50	v=1; $12_{(5,8)} - 11_{(5,7)}$; A
CH_3CHO	232180.27	332	3.6284E-04	50	v=1; $12_{(5,7)} - 11_{(5,6)}$; A
CH_3CHO	231548.63	387	2.8816E-04	50	v=1; $12_{(7,6)} - 11_{(7,5)}$; A
CH_3CHO	231548.63	387	2.8816E-04	50	v=1; $12_{(7,5)} - 11_{(7,4)}$; A
CH_3CHO	231746.68	357	3.2869E-04	50	v=1; $12_{(6,7)} - 11_{(6,6)}$; E
HCOOCH_3	216838.89	106	1.4799E-04	74	v=0; $18_{(2,16)} - 17_{(2,15)}$; A
HCOOCH_3	216967.42	111	1.5319E-04	82	v=0; $20_{(0,20)} - 19_{(0,19)}$; A
HCOOCH_3	216830.20	106	1.4796E-04	74	v=0; $18_{(2,16)} - 17_{(2,15)}$; E
HCOOCH_3	216216.54	109	1.4898E-04	78	v=0; $19_{(1,18)} - 18_{(1,17)}$; A
HCOOCH_3	216115.57	109	1.4875E-04	78	v=0; $19_{(2,18)} - 18_{(2,17)}$; A
HCOOCH_3	216210.91	109	1.4895E-04	78	v=0; $19_{(1,18)} - 18_{(1,17)}$; E
HCOOCH_3	216109.78	109	1.4872E-04	78	v=0; $19_{(2,18)} - 18_{(2,17)}$; E
HCOOCH_3	216969.19	111	2.4436E-05	82	v=0; $20_{(1,20)} - 19_{(0,19)}$; A
HCOOCH_3	216962.99	111	2.4448E-05	82	v=0; $20_{(0,20)} - 19_{(1,19)}$; E
HCOOCH_3	216965.90	111	1.5315E-04	82	v=0; $20_{(1,20)} - 19_{(1,19)}$; A
HCOOCH_3	216966.25	111	1.5313E-04	82	v=0; $20_{(0,20)} - 19_{(0,19)}$; E
HCOOCH_3	216967.99	111	2.4449E-05	82	v=0; $20_{(1,20)} - 19_{(0,19)}$; E
HCOOCH_3	216964.77	111	1.5313E-04	82	v=0; $20_{(1,20)} - 19_{(1,19)}$; E
HCOOCH_3	233777.52	114	1.8391E-04	74	v=0; $18_{(4,14)} - 17_{(4,13)}$; A
HCOOCH_3	233753.96	114	1.8385E-04	74	v=0; $18_{(4,14)} - 17_{(4,13)}$; E
HCOOCH_3	233226.79	123	1.8189E-04	78	v=0; $19_{(4,16)} - 18_{(4,15)}$; A
HCOOCH_3	233628.46	144	1.4443E-05	70	v=0; $17_{(9,9)} - 17_{(8,10)}$; A
HCOOCH_3	233627.48	144	1.4443E-05	70	v=0; $17_{(9,8)} - 17_{(8,9)}$; A
HCOOCH_3	233212.77	123	1.8184E-04	78	v=0; $19_{(4,16)} - 18_{(4,15)}$; E
HCOOCH_3	230315.80	203	1.5394E-05	90	v=0; $22_{(9,14)} - 22_{(8,15)}$; E
HCOOCH_3	233597.70	144	1.4442E-05	70	v=0; $17_{(9,8)} - 17_{(8,9)}$; E
HCOOCH_3	217235.92	368	1.5932E-05	130	v=0; $32_{(9,24)} - 32_{(8,25)}$; E
HCOOCH_3	216114.96	312	1.5134E-05	118	v=0; $29_{(9,20)} - 29_{(8,21)}$; A
HCOOCH_3	233212.77	304	3.8337E-05	78	v=0; $19_{(17,2)} - 18_{(17,1)}$; E
HCOOCH_3	231232.06	264	1.0043E-05	118	v=0; $29_{(4,26)} - 29_{(3,27)}$; E
HCOOCH_3	233394.65	242	8.7967E-05	78	v=0; $19_{(14,5)} - 18_{(14,4)}$; A
HCOOCH_3	233394.65	242	8.7967E-05	78	v=0; $19_{(14,6)} - 18_{(14,5)}$; A
HCOOCH_3	233396.68	242	8.7947E-05	78	v=0; $19_{(14,5)} - 18_{(14,4)}$; E
HCOOCH_3	233504.98	224	1.0245E-04	78	v=0; $19_{(13,6)} - 18_{(13,5)}$; E
HCOOCH_3	233506.69	224	1.0247E-04	78	v=0; $19_{(13,7)} - 18_{(13,6)}$; A
HCOOCH_3	233506.69	224	1.0247E-04	78	v=0; $19_{(13,6)} - 18_{(13,5)}$; A
HCOOCH_3	233524.63	224	1.0250E-04	78	v=0; $19_{(13,7)} - 18_{(13,6)}$; E
HCOOCH_3	233628.46	144	1.4443E-05	70	v=0; $17_{(9,9)} - 17_{(8,10)}$; A
HCOOCH_3	233627.48	144	1.4443E-05	70	v=0; $17_{(9,8)} - 17_{(8,9)}$; A
HCOOCH_3	233655.34	208	1.1599E-04	78	v=0; $19_{(12,8)} - 18_{(12,7)}$; A
$\text{HCOO$					

Table A2 (continued)

Species	<i>f</i> _{rest}	<i>E</i> _u	<i>A</i> _{ij}	<i>g</i> _u	Quantum Numbers
	(MHz)	(K)	(s ⁻¹)		
HCOOCH ₃	233845.23	192	1.2856E-04	78	v=0; 19 _(11,8) – 18 _(11,7) ; E
HCOOCH ₃	233854.29	192	1.2860E-04	78	v=0; 19 _(11,8) – 18 _(11,7) ; A
HCOOCH ₃	233854.29	192	1.2860E-04	78	v=0; 19 _(11,9) – 18 _(11,8) ; A
HCOOCH ₃	231199.35	190	1.5875E-05	86	v=0; 21 _(9,12) – 21 _(8,13) ; A
HCOOCH ₃	231200.14	190	1.5737E-05	86	v=0; 21 _(9,12) – 21 _(8,13) ; E
HCOOCH ₃	232597.28	166	1.5301E-05	78	v=0; 19 _(9,10) – 19 _(8,11) ; E
HCOOCH ₃	233140.74	155	1.4913E-05	74	v=0; 18 _(9,9) – 18 _(8,10) ; E
HCOOCH ₃	233122.16	155	1.4915E-05	74	v=0; 18 _(9,10) – 18 _(8,11) ; E
HCOOCH ₃	233655.34	208	1.1599E-04	78	v=0; 19 _(12,8) – 18 _(12,7) ; A
HCOOCH ₃	233655.34	208	1.1599E-04	78	v=0; 19 _(12,7) – 18 _(12,6) ; A
HCOOCH ₃	216631.08	440	1.5342E-05	146	v=0; 36 _(8,29) – 36 _(7,30) ; E
HCOOCH ₃	231456.84	532	1.7389E-05	162	v=0; 40 _(7,33) – 40 _(6,34) ; A
HCOOCH ₃	217262.88	485	1.6574E-05	150	v=0; 37 _(10,27) – 37 _(9,28) ; A
HCOOCH ₃	231469.66	441	1.9260E-05	142	v=0; 35 _(10,25) – 35 _(9,26) ; E
HCOOCH ₃	219822.13	355	1.1074E-04	74	v=1; 18 _(10,9) – 17 _(10,8) ; A
HCOOCH ₃	219822.13	355	1.1074E-04	74	v=1; 18 _(10,8) – 17 _(10,7) ; A
HCOOCH ₃	232164.44	366	1.3664E-04	78	v=1; 19 _(10,9) – 18 _(10,8) ; A
HCOOCH ₃	232164.44	366	1.3664E-04	78	v=1; 19 _(10,10) – 18 _(10,9) ; A
HCOOCH ₃	231749.76	366	1.3589E-04	78	v=1; 19 _(10,9) – 18 _(10,8) ; E
HCOOCH ₃	231230.68	396	1.1221E-04	78	v=1; 19 _(12,7) – 18 _(12,6) ; E
HCOOCH ₃	232422.05	404	1.6823E-05	94	v=1; 23 _(9,15) – 23 _(8,16) ; E
HCOOCH ₃	232077.29	404	1.6897E-05	94	v=1; 23 _(9,15) – 23 _(8,16) ; A
HCOOCH ₃	231846.82	412	1.0029E-04	78	v=1; 19 _(13,6) – 18 _(13,5) ; A
HCOOCH ₃	231846.82	412	1.0029E-04	78	v=1; 19 _(13,7) – 18 _(13,6) ; A
HCOOCH ₃	231270.76	418	1.6910E-05	98	v=1; 24 _(9,16) – 24 _(8,17) ; E
HCOOCH ₃	231816.99	430	8.6209E-05	78	v=1; 19 _(14,6) – 18 _(14,5) ; A
HCOOCH ₃	231816.99	430	8.6209E-05	78	v=1; 19 _(14,5) – 18 _(14,4) ; A
HCOOCH ₃	217241.80	477	1.0797E-05	122	v=1; 30 _(5,26) – 30 _(4,27) ; E
HCOOCH ₃	231278.96	493	3.7401E-05	78	v=1; 19 _(17,3) – 18 _(17,2) ; E
HCOOCH ₃	231149.58	516	1.9188E-05	78	v=1; 19 _(18,2) – 18 _(18,1) ; E
HCOOCH ₃	231467.34	562	1.4832E-05	138	v=1; 34 _(6,29) – 34 _(5,30) ; A
HCOOCH ₃	233600.06	647	1.9970E-05	146	v=1; 36 _(10,26) – 36 _(9,27) ; A
HCOOCH ₃	233142.48	949	1.9936E-05	194	v=1; 48 _(9,39) – 48 _(8,40) ; A
HCOOCH ₃	218762.13	1050	1.7906E-05	206	v=1; 51 _(10,41) – 51 _(9,42) ; A
HCOOCH ₃	232423.45	353	1.4701E-04	78	v=1; 19 _(9,11) – 18 _(9,10) ; A
HCOOCH ₃	232423.45	353	1.4701E-04	78	v=1; 19 _(9,10) – 18 _(9,9) ; A
HCOOCH ₃	233080.84	353	1.4869E-04	78	v=1; 19 _(9,11) – 18 _(9,10) ; E
HCOOCH ₃	233627.48	341	1.5875E-04	78	v=1; 19 _(8,12) – 18 _(8,11) ; E
HCOOCH ₃	233598.10	332	1.6650E-04	78	v=1; 19 _(7,12) – 18 _(7,11) ; E
HCOOCH ₃	233487.68	332	1.6589E-04	78	v=1; 19 _(7,13) – 18 _(7,12) ; A
HCOOCH ₃	231245.42	310	1.7698E-04	78	v=1; 19 _(4,16) – 18 _(4,15) ; A
HCOOCH ₃	231724.16	301	1.7932E-04	74	v=1; 18 _(4,14) – 17 _(4,13) ; E
HCOOCH ₃	215837.59	299	1.5046E-04	82	v=1; 20 _(1,20) – 19 _(1,19) ; A
HCOOCH ₃	215839.54	299	1.5046E-04	82	v=1; 20 _(0,20) – 19 _(0,19) ; A
HCOOCH ₃	215891.90	298	1.5126E-04	82	v=1; 20 _(1,20) – 19 _(1,19) ; E
HCOOCH ₃	215889.66	298	2.3710E-05	82	v=1; 20 _(0,20) – 19 _(1,19) ; E
HCOOCH ₃	215893.71	298	1.5126E-04	82	v=1; 20 _(0,20) – 19 _(0,19) ; E
CH ₂ (OH)CHO	231724.33	42	2.5438E-04	17	8 _(6,2) – 7 _(5,3)
CH ₂ (OH)CHO	231723.27	42	2.5438E-04	17	8 _(6,3) – 7 _(5,2)
CH ₂ (OH)CHO	233797.25	95	1.3045E-04	35	17 _(4,14) – 16 _(3,13)
CH ₂ (OH)CHO	232335.45	135	3.0669E-04	45	22 _(2,21) – 21 _(1,20)
CH ₂ (OH)CHO	232286.03	135	3.0656E-04	45	22 _(1,21) – 21 _(2,20)
CH ₂ (OH)CHO	233037.73	137	3.6542E-04	47	23 _(1,23) – 22 _(0,22)

Table A2 (continued)

Species	<i>f</i> _{rest}	<i>E</i> _u	<i>A</i> _{ij}	<i>g</i> _u	Quantum Numbers
	(MHz)	(K)	(s ⁻¹)		
CH ₂ (OH)CHO	233037.36	137	3.6542E-04	47	23 _(0,23) – 22 _(1,22)
CH ₂ (OH)CHO	232288.41	271	2.0576E-04	55	27 _(10,17) – 27 _(9,18)
CH ₂ (OH)CHO	231200.38	287	2.0649E-04	57	28 _(10,19) – 28 _(9,20)
CH ₂ (OH)CHO	232782.05	804	4.7057E-05	99	49 _(14,35) – 48 _(15,34)
CH ₂ (OH)CHO	233037.73	137	3.6542E-04	47	23 _(1,23) – 22 _(0,22)
CH ₂ (OH)CHO	233037.36	137	3.6542E-04	47	23 _(0,23) – 22 _(1,22)
CH ₃ COCH ₃	233601.55	122	3.5806E-04	370	18 _(7,12) – 17 _(6,11) ; AA
CH ₃ COCH ₃	218127.21	119	2.2105E-04	656	20 _(3,18) – 19 _(2,17) ; EE
CH ₃ COCH ₃	218127.21	119	2.2105E-04	656	20 _(2,18) – 19 _(3,17) ; EE
CH ₃ COCH ₃	230182.81	220	4.2074E-05	912	28 _(3,26) – 28 _(2,27) ; EE
CH ₃ COCH ₃	230182.81	220	4.2074E-05	912	28 _(2,26) – 28 _(1,27) ; EE
CH ₃ COCH ₃	217022.51	115	3.8943E-04	624	19 _(3,16) – 18 _(4,15) ; EE
CH ₃ COCH ₃	217022.51	115	3.8943E-04	624	19 _(4,16) – 18 _(3,15) ; EE
CH ₃ COCH ₃	232962.37	115	2.9451E-04	210	17 _(8,10) – 16 _(7,9) ; AA
CH ₃ COCH ₃	218127.21	119	2.2105E-04	656	20 _(3,18) – 19 _(2,17) ; EE
CH ₃ COCH ₃	218127.21	119	2.2105E-04	656	20 _(2,18) – 19 _(3,17) ; EE
CH ₃ COCH ₃	230990.98	172	2.8660E-05	410	20 _(13,8) – 19 _(14,5) ; AA
CH ₃ COCH ₃	219242.14	122	3.8802E-05	688	21 _(2,20) – 20 _(1,19) ; EE
CH ₃ COCH ₃	219242.14	122	3.8802E-05	688	21 _(1,20) – 20 _(2,19) ; EE
CH ₃ COCH ₃	232181.92	381	1.0944E-05	976	30 _(19,11) – 30 _(16,14) ; EE
CH ₃ COCH ₃	218221.72	717	2.3951E-05	154	38 _(38,0) – 38 _(37,1) ; AE
CH ₃ COCH ₃	218221.72	717	2.3950E-05	462	38 _(38,1) – 38 _(37,2) ; AE
CH ₃ COCH ₃	219242.14	122	4.3148E-04	688	21 _(1,20) – 20 _(1,19) ; EE
CH ₃ COCH ₃	219242.14	122	4.3148E-04	688	21 _(2,20) – 20 _(2,19) ; EE
CH ₃ COCH ₃	218281.37	899	2.4303E-04	582	48 _(22,26) – 48 _(21,27) ; AA
CH ₃ COCH ₃	218281.38	899	2.4301E-04	970	48 _(23,26) – 48 _(22,27) ; AA
CH ₃ COCH ₃	217240.80	900	1.1949E-04	356	44 _(39,6) – 44 _(38,7) ; EA
CH ₃ COCH ₃	231738.68	922	9.7698E-05	356	44 _(41,4) – 44 _(40,5) ; EA
CH ₃ COCH ₃	215892.02	932	1.3305E-04	910	45 _(39,6) – 45 _(38,7) ; AA
CH ₃ COCH ₃	231199.96	765	3.7119E-04	1456	45 _(18,27) – 45 _(17,28) ; EE
CH ₃ COCH ₃	231199.96	765	3.7119E-04	1456	45 _(19,27) – 45 _(18,28) ; EE
CH ₃ COCH ₃	230183.08	135	5.8067E-04	282	23 _(1,23) – 22 _(0,22) ; AA
CH ₃ COCH ₃	215892.02	932	1.3303E-04	546	45 _(39,7) – 45 _(38,8) ; AA
CH ₃ COCH ₃	230183.08	135	5.8061E-04	470	23 _(0,23) – 22 _(1,22) ; AA
CH ₃ COCH ₃	230176.73	135	1.2709E-04	752	23 _(1,23) – 22 _(1,22) ; EE
CH ₃ COCH ₃	230176.73	135	1.2709E-04	752	23 _(0,23) – 22 _(0,22) ; EE
CH ₃ COCH ₃	233600.13	122	3.5802E-04	222	18 _(6,12) – 17 _(7,11) ; AA
CH ₃ COCH ₃	230176.73	135	1.2709E-04	752	23 _(1,23) – 22 _(1,22) ; EE
CH ₃ COCH ₃	230176.73	135	1.2709E-04	752	23 _(0,23) – 22 _(0,22) ; EE
CH ₃ COCH ₃	230176.73	135	4.5352E-04	752	23 _(1,23) – 22 _(0,22) ; EE
CH ₃ COCH ₃	230176.73	135	4.5352E-04	752	23 _(0,23) – 22 _(1,22) ; EE
CH ₃ COCH ₃	230182.81	220	4.2074E-05	912	28 _(3,26) – 28 _(2,27) ; EE
CH ₃ COCH ₃	230182.81	220	4.2074E-05	912	28 _(2,26) – 28 _(1,27) ; EE
HNCO	219798.27	58	1.4693E-04	21	10 _(0,10) – 9 _(0,9)
HNCO	218981.01	101	1.4222E-04	21	10 _(1,10) – 9 _(1,9)
HNCO	219733.85	228	1.3458E-04	21	10 _(2,9) – 9 _(2,8)
HNCO	219737.19	228	1.3458E-04	21	10 _(2,8) – 9 _(2,7)
HNCO	219656.77	433	1.2012E-04	21	10 _(3,8) – 9 _(3,7)
HNCO	219656.77	433	1.2012E-04	21	10 _(3,7) – 9 _(3,6)
HNCO	231873.26	470	6.6812E-05	57	28 _(1,28) – 29 _(0,29)
¹³ CH ₃ CN	232194.91	142	1.0217E-03	54	13 ₃ – 12 ₃ ; A2-A1
¹³ CH ₃ CN	232194.91	142	1.0217E-03	54	13 ₃ – 12 ₃ ; A1-A2
¹³ CH ₃ CN	23207				

Table A2 (*continued*)

Species	f_{rest}	E_u	A_{ij}	g_u	Quantum Numbers	$C_{215}\text{CN}$	233208.03	434	0.0093E-04	53	$20(16,10) - 25(16,9)$
	(MHz)	(K)	(s^{-1})			$C_2\text{H}_5\text{CN}$	233208.03	434	6.6695E-04	53	$26(16,11) - 25(16,10)$
$^{13}\text{CH}_3\text{CN}$	232077.20	336	8.4805E-04	54	$13_6 - 12_6$; A2-A1	HCCCN	218324.72	131	8.2613E-04	49	$24 - 23$
$^{13}\text{CH}_3\text{CN}$	232194.91	142	1.0217E-03	54	$13_3 - 12_3$; A2-A1	NH_2CHO	233488.89	258	4.3644E-04	23	$11_{(8,3)} - 10_{(8,2)}$
$^{13}\text{CH}_3\text{CN}$	232194.91	142	1.0217E-03	54	$13_3 - 12_3$; A1-A2	NH_2CHO	233488.89	258	4.3644E-04	23	$11_{(8,4)} - 10_{(8,3)}$
$\text{C}_2\text{H}_5\text{CN}$	231269.83	1056	1.4160E-05	117	$58_{(17,42)} - 59_{(16,43)}$	NH_2CHO	233505.52	365	1.6086E-04	23	$11_{(10,1)} - 10_{(10,0)}$
$\text{C}_2\text{H}_5\text{CN}$	231269.83	1056	1.4160E-05	117	$58_{(17,41)} - 59_{(16,44)}$	NH_2CHO	233505.52	365	1.6086E-04	23	$11_{(10,2)} - 10_{(10,1)}$
$\text{C}_2\text{H}_5\text{CN}$	233069.31	205	9.9390E-04	53	$26_{(7,20)} - 25_{(7,19)}$	NH_2CHO	233492.68	308	3.0630E-04	23	$11_{(9,2)} - 10_{(9,1)}$
$\text{C}_2\text{H}_5\text{CN}$	233069.38	205	9.9390E-04	53	$26_{(7,19)} - 25_{(7,18)}$	NH_2CHO	233492.68	308	3.0630E-04	23	$11_{(9,3)} - 10_{(9,2)}$
$\text{C}_2\text{H}_5\text{CN}$	233205.09	191	1.0164E-03	53	$26_{(6,21)} - 25_{(6,20)}$	NH_2CHO	233896.58	94	8.6203E-04	23	$11_{(3,9)} - 10_{(3,8)}$
$\text{C}_2\text{H}_5\text{CN}$	233498.30	179	1.0375E-03	53	$26_{(5,21)} - 25_{(5,20)}$	NH_2CHO	233498.07	213	5.5141E-04	23	$11_{(7,4)} - 10_{(7,3)}$
$\text{C}_2\text{H}_5\text{CN}$	233654.02	169	1.0540E-03	53	$26_{(4,23)} - 25_{(4,22)}$	NH_2CHO	233498.07	213	5.5141E-04	23	$11_{(7,5)} - 10_{(7,4)}$
$\text{C}_2\text{H}_5\text{CN}$	231312.30	158	9.1831E-05	55	$27_{(0,27)} - 26_{(1,26)}$	NH_2CHO	233527.80	174	6.5125E-04	23	$11_{(6,6)} - 10_{(6,5)}$
$\text{C}_2\text{H}_5\text{CN}$	232998.74	222	9.6916E-04	53	$26_{(8,19)} - 25_{(8,18)}$	NH_2CHO	233527.80	174	6.5125E-04	23	$11_{(6,5)} - 10_{(6,4)}$
$\text{C}_2\text{H}_5\text{CN}$	232998.74	222	9.6916E-04	53	$26_{(8,18)} - 25_{(8,17)}$	NH_2CHO	233594.50	142	7.3618E-04	23	$11_{(5,7)} - 10_{(5,6)}$
$\text{C}_2\text{H}_5\text{CN}$	232967.57	241	9.4197E-04	53	$26_{(9,17)} - 25_{(9,16)}$	NH_2CHO	233594.50	142	7.3618E-04	23	$11_{(5,6)} - 10_{(5,5)}$
$\text{C}_2\text{H}_5\text{CN}$	232967.57	241	9.4197E-04	53	$26_{(9,18)} - 25_{(9,17)}$	NH_2CHO	233734.72	115	8.0662E-04	23	$11_{(4,8)} - 10_{(4,7)}$
$\text{C}_2\text{H}_5\text{CN}$	232967.57	241	9.4197E-04	53	$26_{(9,17)} - 25_{(9,16)}$	NH_2CHO	232273.65	79	8.8167E-04	23	$11_{(2,10)} - 10_{(2,9)}$
$\text{C}_2\text{H}_5\text{CN}$	232967.57	241	9.4197E-04	53	$26_{(9,18)} - 25_{(9,17)}$	NH_2CHO	215687.01	68	6.9810E-04	21	$10_{(2,8)} - 9_{(2,7)}$
$\text{C}_2\text{H}_5\text{CN}$	232967.57	241	9.4197E-04	53	$26_{(9,17)} - 25_{(9,16)}$	NH_2CHO	218459.21	61	7.4751E-04	21	$10_{(1,9)} - 9_{(1,8)}$
$\text{C}_2\text{H}_5\text{CN}$	232967.57	241	9.4197E-04	53	$26_{(9,18)} - 25_{(9,17)}$	NH_2CHO	233498.07	213	5.5141E-04	23	$11_{(7,4)} - 10_{(7,3)}$
$\text{C}_2\text{H}_5\text{CN}$	231269.83	1056	1.4160E-05	117	$58_{(17,42)} - 59_{(16,43)}$	NH_2CHO	233498.07	213	5.5141E-04	23	$11_{(7,5)} - 10_{(7,4)}$
$\text{C}_2\text{H}_5\text{CN}$	231269.83	1056	1.4160E-05	117	$58_{(17,41)} - 59_{(16,44)}$	OCS	218903.36	100	3.0384E-05	37	$18 - 17$
$\text{C}_2\text{H}_5\text{CN}$	232286.30	738	5.6326E-05	115	$57_{(4,53)} - 57_{(3,54)}$	OCS	231060.99	111	3.5783E-05	39	$19 - 18$
$\text{C}_2\text{H}_5\text{CN}$	232962.32	262	9.1185E-04	53	$26_{(10,16)} - 25_{(10,15)}$						
$\text{C}_2\text{H}_5\text{CN}$	232962.32	262	9.1185E-04	53	$26_{(10,17)} - 25_{(10,16)}$						
$\text{C}_2\text{H}_5\text{CN}$	233523.50	592	4.4001E-04	53	$26_{(20,7)} - 25_{(20,6)}$						
$\text{C}_2\text{H}_5\text{CN}$	233523.50	592	4.4001E-04	53	$26_{(20,6)} - 25_{(20,5)}$						
$\text{C}_2\text{H}_5\text{CN}$	233523.50	592	4.4001E-04	53	$26_{(20,7)} - 25_{(20,6)}$						
$\text{C}_2\text{H}_5\text{CN}$	233523.50	592	4.4001E-04	53	$26_{(20,6)} - 25_{(20,5)}$						

B. SUPPLEMENTARY IMAGES

Figure B1 shows supplementary images of this study.

REFERENCES

Arce, H. G., Santiago-Garcia, J., Jorgensen, J. K., Tafalla, M., & Bachiller, R. 2008, *Astrophysical Journal Letters*, 681, L21, doi: [10.1086/590110](https://doi.org/10.1086/590110)

Astropy Collaboration, Robitaille, T. P., Tollerud, E. J., et al. 2013, *A&A*, 558, A33, doi: [10.1051/0004-6361/201322068](https://doi.org/10.1051/0004-6361/201322068)

Astropy Collaboration, Price-Whelan, A. M., Lim, P. L., et al. 2022, *ApJ*, 935, 167, doi: [10.3847/1538-4357/ac7c74](https://doi.org/10.3847/1538-4357/ac7c74)

Belloche, A., Maury, A. J., Maret, S., et al. 2020, *A&A*, 635, A198, doi: [10.1051/0004-6361/201937352](https://doi.org/10.1051/0004-6361/201937352)

Bianchi, E., Lopez-Sepulcre, A., Ceccarelli, C., et al. 2022, *Astrophysical Journal Letters*, 928, L3, doi: [10.3847/2041-8213/ac5a56](https://doi.org/10.3847/2041-8213/ac5a56)

Bianchi, E., Codella, C., Ceccarelli, C., et al. 2019, *Monthly Notices of the Royal Astronomical Society*, 483, 1850, doi: [10.1093/mnras/sty2915](https://doi.org/10.1093/mnras/sty2915)

Bianchi, E., Chandler, C. J., Ceccarelli, C., et al. 2020, *Monthly Notices of the Royal Astronomical Society: Letters*, 498, L87, doi: [10.1093/mnrasl/slaa130](https://doi.org/10.1093/mnrasl/slaa130)

Bouvier, M., Ceccarelli, C., López-Sepulcre, A., et al. 2022, *ApJ*, 929, 10, doi: [10.3847/1538-4357/ac5904](https://doi.org/10.3847/1538-4357/ac5904)

Bouvier, M., Giani, L., Chahine, L., et al. 2025, *MNRAS*, 539, 2380, doi: [10.1093/mnras/staf631](https://doi.org/10.1093/mnras/staf631)

Busch, L. A., Pineda, J. E., Sipilä, O., et al. 2025, *A&A*, 699, A359, doi: [10.1051/0004-6361/202554104](https://doi.org/10.1051/0004-6361/202554104)

CASA Team, Bean, B., Bhatnagar, S., et al. 2022, *Publications of the Astronomical Society of the Pacific*, 134, 114501, doi: [10.1088/1538-3873/ac9642](https://doi.org/10.1088/1538-3873/ac9642)

Ceccarelli, C. 2004, in *Star Formation in the Interstellar Medium: In Honor of David Hollenbach, Chris McKee and Frank Shu, ASP Conference Proceeding*, ed. D. Johnstone, F. Adams, D. Lin, D. Neufeld, & E. Ostriker, Vol. 323, San Francisco, Astronomical Society of the Pacific (ASP Conference Proceedings)

Ceccarelli, C., Codella, C., Balucani, N., et al. 2023, in *Astronomical Society of the Pacific Conference Series*, Vol. 534, *Protostars and Planets VII*, ed. S. Inutsuka, Y. Aikawa, T. Muto, K. Tomida, & M. Tamura, 379

Codella, C., Ceccarelli, C., Cabrit, S., et al. 2016, *A&A*, 586, L3, doi: [10.1051/0004-6361/201527424](https://doi.org/10.1051/0004-6361/201527424)

Comrie, A., Wang, K.-S., Hsu, S.-C., et al. 2021, *Astrophysics Source Code Library*, ascl:2103.031. <https://ui.adsabs.harvard.edu/abs/2021ascl.soft03031C>

De Simone, M., Ceccarelli, C., Codella, C., et al. 2020, *ApJ*, 896, L3, doi: [10.3847/2041-8213/ab8d41](https://doi.org/10.3847/2041-8213/ab8d41)

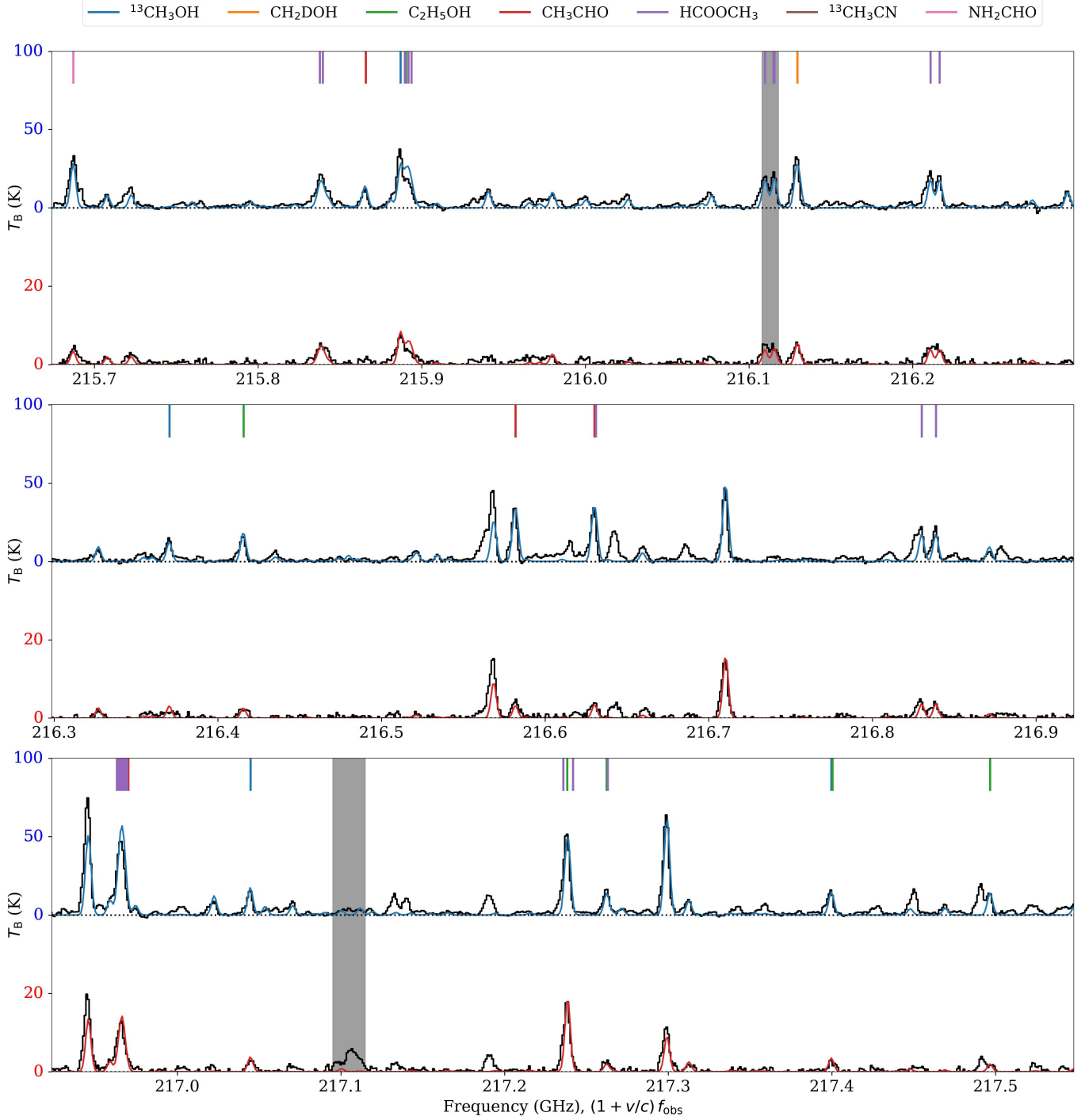


Figure A1. Observed and synthesized spectra. Each panel is divided into two parts: the upper part corresponds to HOPS-288-A and the lower part to HOPS-288-B. The black spectra show the observation results, while the blue and red curves represent the synthesized spectra for HOPS-288-A and HOPS-288-B, respectively. Shaded regions indicate frequency ranges excluded from the fitting due to known transitions with non-Gaussian profiles, including CO, C¹⁸O, SiO, and DCO⁺. Short vertical ticks at the top of each panel mark the selected COM transitions. The x-axis shows frequency shifted to the expected rest frame using $v = 2.0 \text{ km s}^{-1}$ and $v = 6.5 \text{ km s}^{-1}$ for HOPS-288-A and HOPS-288-B, respectively.

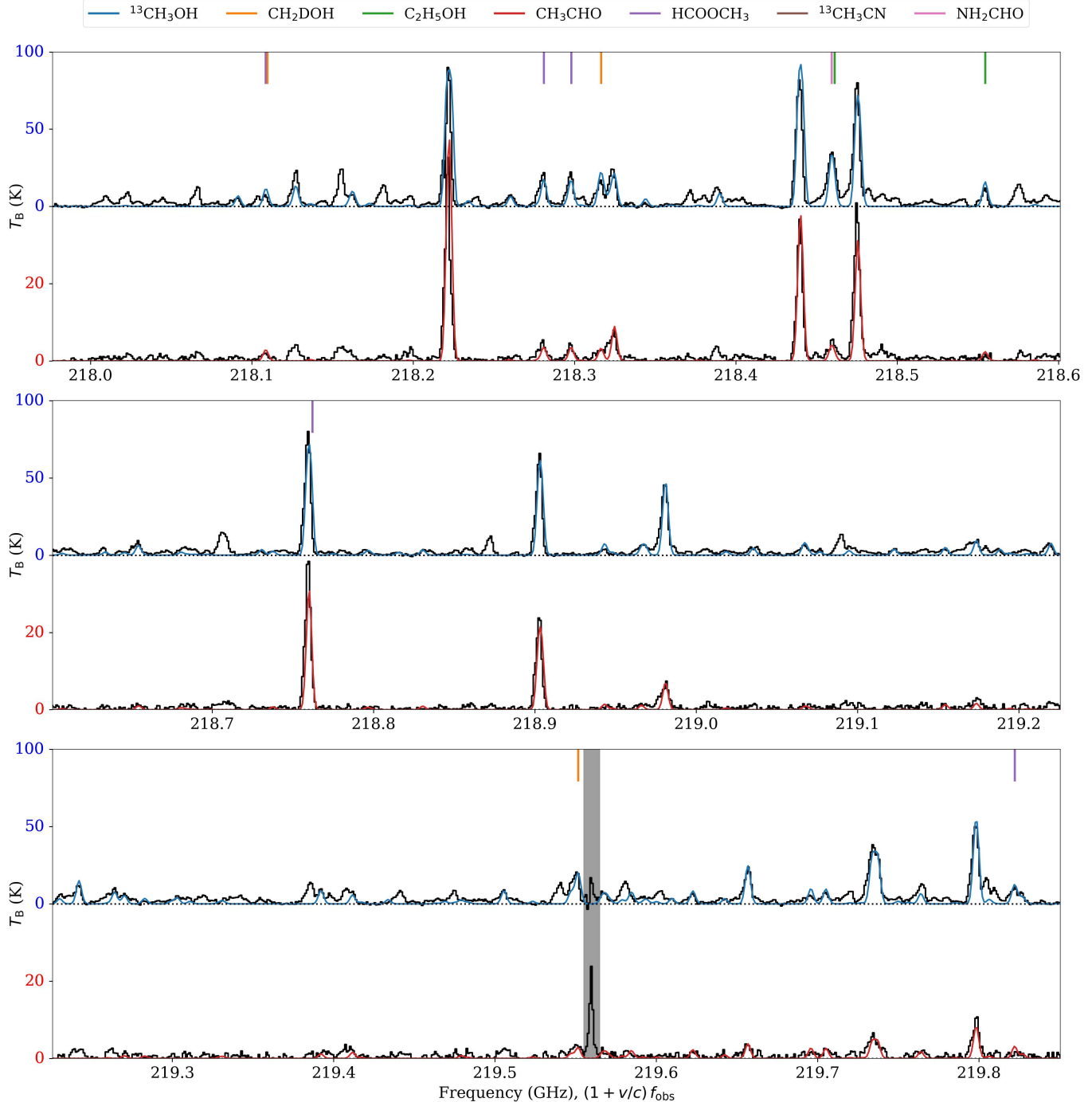


Figure A2. The captions follow Figure A1 with different frequency ranges.

Dutta, S., Lee, C.-F., Johnstone, D., et al. 2022, *ApJ*, 925, 11,

doi: [10.3847/1538-4357/ac3424](https://doi.org/10.3847/1538-4357/ac3424)

—. 2024, *The Astronomical Journal*, 167, 72,

doi: [10.3847/1538-3881/ad152b](https://doi.org/10.3847/1538-3881/ad152b)

Fadul, A. M. A., Schwarz, K. R., van 't Hoff, M. L. R., et al. 2025,

arXiv e-prints, arXiv:2504.06005,

doi: [10.48550/arXiv.2504.06005](https://doi.org/10.48550/arXiv.2504.06005)

Frediani, J., De Simone, M., Testi, L., et al. 2025, *A&A*, 695, A78,

doi: [10.1051/0004-6361/202452191](https://doi.org/10.1051/0004-6361/202452191)

Furlan, E., Fischer, W. J., Ali, B., et al. 2016, *ApJS*, 224, 5,

doi: [10.3847/0067-0049/224/1/5](https://doi.org/10.3847/0067-0049/224/1/5)

Hsieh, C.-H., Arce, H. G., Li, Z.-Y., et al. 2023a, *ApJ*, 947, 25,

doi: [10.3847/1538-4357/acba13](https://doi.org/10.3847/1538-4357/acba13)

Hsieh, T. H., Segura-Cox, D. M., Pineda, J. E., et al. 2023b, *A&A*,

669, A137, doi: [10.1051/0004-6361/202244183](https://doi.org/10.1051/0004-6361/202244183)

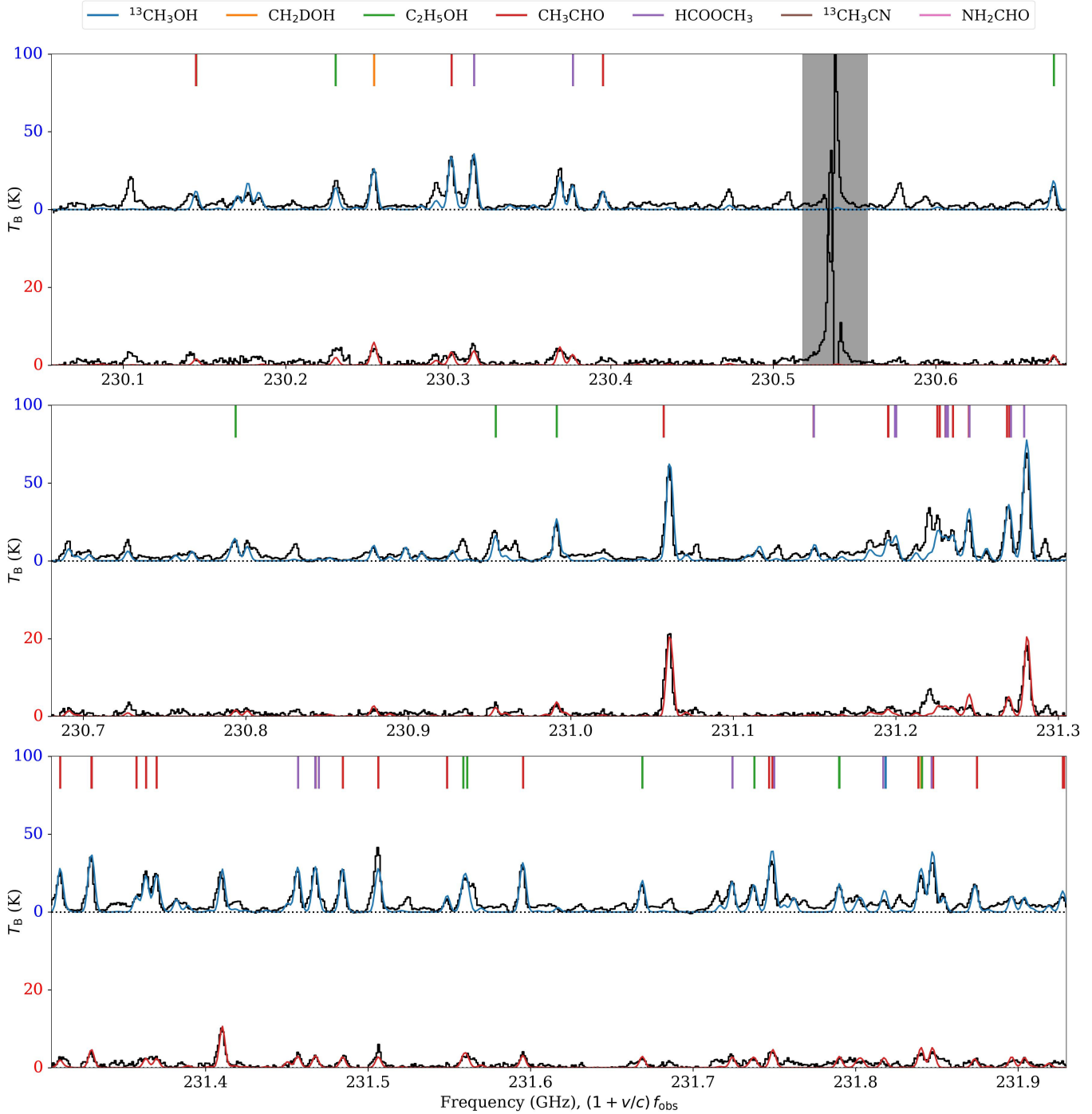


Figure A3. The captions follow Figure A1 with different frequency ranges.

Hsieh, T. H., Pineda, J. E., Segura-Cox, D. M., et al. 2024, A&A, 686, A289, doi: [10.1051/0004-6361/202449417](https://doi.org/10.1051/0004-6361/202449417)

Hsieh, T. H., Pineda, J. E., Segura-Cox, D. M., et al. 2025, A&A, 696, A1, doi: [10.1051/0004-6361/202453273](https://doi.org/10.1051/0004-6361/202453273)

Hsu, S.-Y., Liu, S.-Y., Liu, T., et al. 2020, ApJ, 898, 107, doi: [10.3847/1538-4357/ab9f3a](https://doi.org/10.3847/1538-4357/ab9f3a)

—. 2022, ApJ, 927, 218, doi: [10.3847/1538-4357/ac49e0](https://doi.org/10.3847/1538-4357/ac49e0)

Hsu, S.-Y., Liu, S.-Y., Johnstone, D., et al. 2023, ApJ, 956, 120, doi: [10.3847/1538-4357/acefcf](https://doi.org/10.3847/1538-4357/acefcf)

Hsu, S.-Y., Lee, C.-F., Liu, S.-Y., et al. 2024, ApJ, 976, 29, doi: [10.3847/1538-4357/ad7e25](https://doi.org/10.3847/1538-4357/ad7e25)

Hsu, S.-Y., Liu, S.-Y., Liu, X., et al. 2025, ApJ, 984, L58, doi: [10.3847/2041-8213/adcd6a](https://doi.org/10.3847/2041-8213/adcd6a)

Hsu, S.-Y., Lee, C.-F., Johnstone, D., et al. 2025, ApJ, 989, 56, doi: [10.3847/1538-4357/ade7fc](https://doi.org/10.3847/1538-4357/ade7fc)

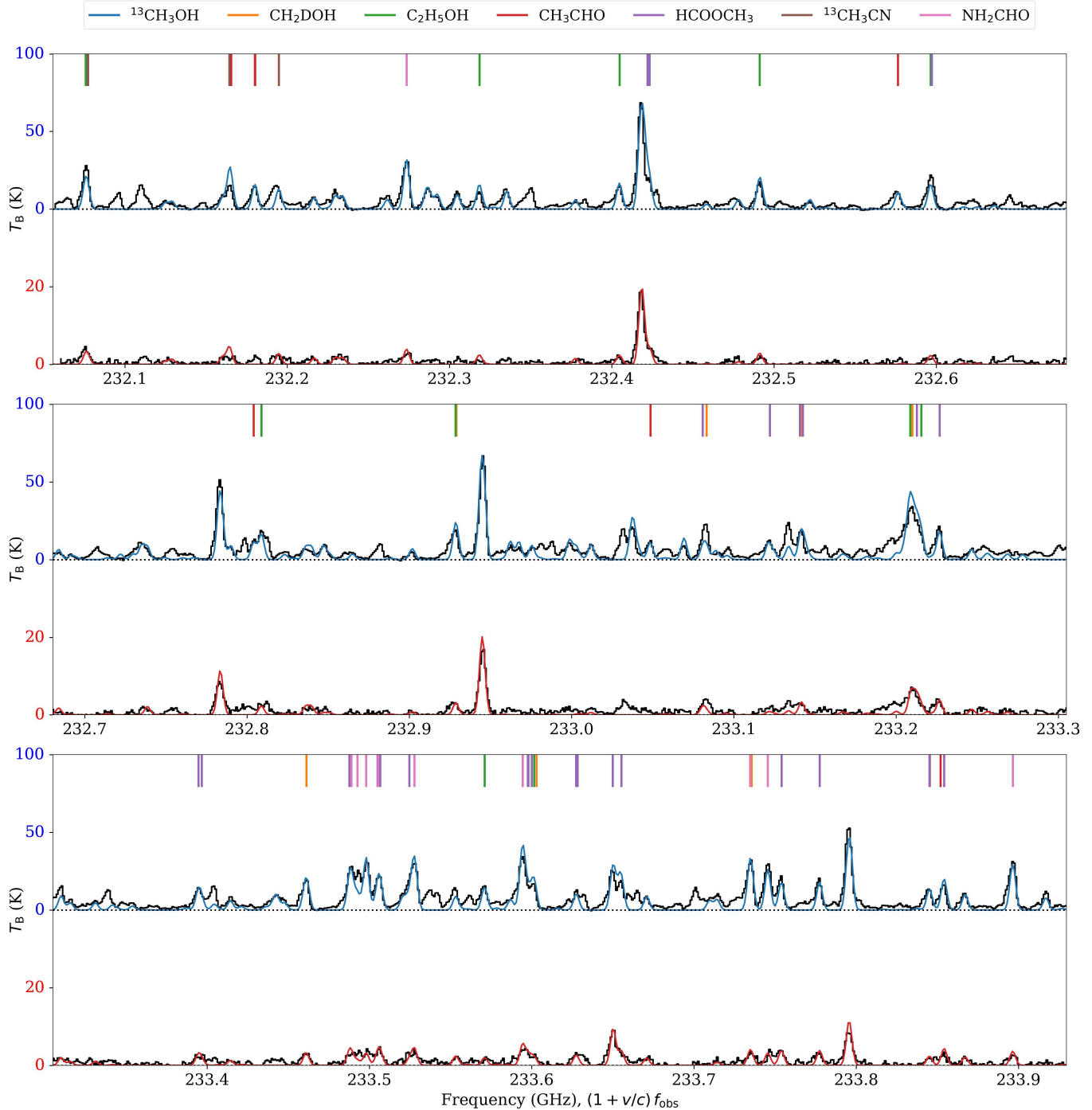


Figure A4. The captions follow Figure A1 with different frequency ranges.

Jacobsen, S. K., Jørgensen, J. K., Di Francesco, J., et al. 2019, *A&A*, 629, A29, doi: [10.1051/0004-6361/201833214](https://doi.org/10.1051/0004-6361/201833214)
 Jeong, J.-H., Lee, J.-E., Lee, S., et al. 2025, *ApJS*, 276, 49, doi: [10.3847/1538-4365/ad9450](https://doi.org/10.3847/1538-4365/ad9450)
 Jørgensen, J. K., van der Wiel, M. H. D., Coutens, A., et al. 2016, *A&A*, 595, A117, doi: [10.1051/0004-6361/201628648](https://doi.org/10.1051/0004-6361/201628648)
 Jørgensen, J. K., Müller, H. S. P., Calcutt, H., et al. 2018, *A&A*, 620, A170, doi: [10.1051/0004-6361/201731667](https://doi.org/10.1051/0004-6361/201731667)

Kim, G., Tatematsu, K., Liu, T., et al. 2020, *ApJS*, 249, 33, doi: [10.3847/1538-4365/aba746](https://doi.org/10.3847/1538-4365/aba746)
 Lee, C. F., Codella, C., Ceccarelli, C., & Lopez-Sepulcre, A. 2022, *Astrophysical Journal*, 937, 10, doi: [10.3847/1538-4357/ac8c28](https://doi.org/10.3847/1538-4357/ac8c28)
 Lee, C.-F., Codella, C., Li, Z.-Y., & Liu, S.-Y. 2019a, *ApJ*, 876, 63, doi: [10.3847/1538-4357/ab15db](https://doi.org/10.3847/1538-4357/ab15db)
 Lee, C.-F., Li, Z.-Y., Ho, P. T. P., et al. 2017, *ApJ*, 843, 27, doi: [10.3847/1538-4357/aa7757](https://doi.org/10.3847/1538-4357/aa7757)

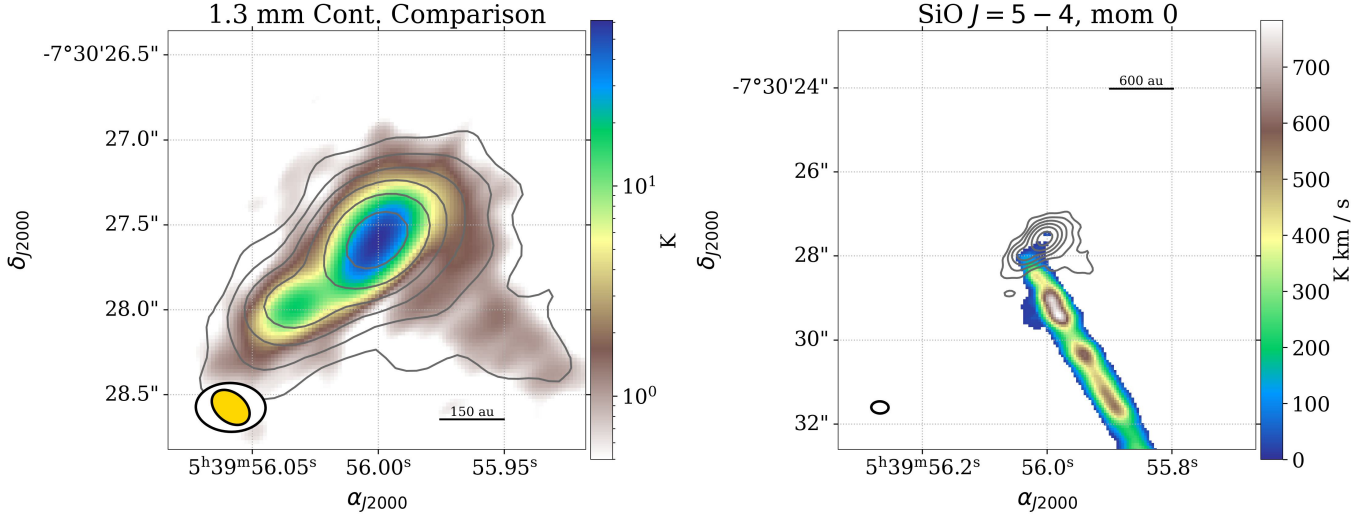


Figure B1. The selected images of dust continuum or integrated intensity of molecular transitions. The ellipses at the bottom left corner illustrate the observation beam(s), yellow for ALMA #2018.1.01038.S (high resolution) and white for #2018.1.00302.S (wide bandwidth). Panel (a): the comparisons of the 1.3 mm (230 GHz) dust continuum between the two programs used in this study. Comparisons of the 1.3 mm dust continuum observed by the high-resolution (color scale) and the wide-coverage (grey contours) data. The contour levels are $[5, 10, 20, 40, 80, 160]\sigma$, where σ is 0.13 K. Panel (b): The SiO $J = 5 - 4$ integrated intensity ($-15.5 - 24.5 \text{ km s}^{-1}$) overlaid with 1.3 mm (230 GHz) dust continuum, both obtained from the wide coverage data. The contour levels are $[5, 10, 20, 40, 80, 160]\sigma$, where σ is 0.13 K. A mask of 5σ was applied during the integration.

Lee, J.-E., Lee, S., Baek, G., et al. 2019b, *Nature Astronomy*, 3, 314, doi: [10.1038/s41550-018-0680-0](https://doi.org/10.1038/s41550-018-0680-0)

Lee, J.-E., Baek, G., Lee, S., et al. 2023, *The Astrophysical Journal*, 956, 43, doi: [10.3847/1538-4357/ace34b](https://doi.org/10.3847/1538-4357/ace34b)

Liu, H. B., Tsai, A.-L., Chen, W. P., et al. 2021, *ApJ*, 923, 270, doi: [10.3847/1538-4357/ac31b9](https://doi.org/10.3847/1538-4357/ac31b9)

Lombardi, M., Alves, J., & Lada, C. J. 2011, *A&A*, 535, A16, doi: [10.1051/0004-6361/201116915](https://doi.org/10.1051/0004-6361/201116915)

Louvet, F., Dougados, C., Cabrit, S., et al. 2018, *A&A*, 618, A120, doi: [10.1051/0004-6361/201731733](https://doi.org/10.1051/0004-6361/201731733)

López-Sepulcre, A., Balucani, N., Ceccarelli, C., et al. 2019, *ACS Earth and Space Chemistry*, 3, 2122, doi: [10.1021/acsearthspacechem.9b00154](https://doi.org/10.1021/acsearthspacechem.9b00154)

López-Sepulcre, A., Codella, C., Ceccarelli, C., Podio, L., & Robuschi, J. 2024, *arXiv e-prints*, arXiv:2411.00495, doi: [10.48550/arXiv.2411.00495](https://doi.org/10.48550/arXiv.2411.00495)

López-Sepulcre, A., Sakai, N., Neri, R., et al. 2017, *A&A*, 606, A121, doi: [10.1051/0004-6361/201630334](https://doi.org/10.1051/0004-6361/201630334)

Manigand, S., Jorgensen, J. K., Calcutt, H., et al. 2020, *A&A*, 635, A48, doi: [10.1051/0004-6361/201936299](https://doi.org/10.1051/0004-6361/201936299)

Martín-Doménech, R., Bergner, J. B., Öberg, K. I., et al. 2021, *ApJ*, 923, 155, doi: [10.3847/1538-4357/ac26b9](https://doi.org/10.3847/1538-4357/ac26b9)

Martín-Doménech, R., Öberg, K. I., & Rajappan, M. 2020, *ApJ*, 894, 98, doi: [10.3847/1538-4357/ab84e8](https://doi.org/10.3847/1538-4357/ab84e8)

Milam, S. N., Savage, C., Brewster, M. A., Ziurys, L. M., & Wyckoff, S. 2005, *The Astrophysical Journal*, 634, 1126, doi: [10.1086/497123](https://doi.org/10.1086/497123)

Möller, T., Endres, C., & Schilke, P. 2017, *A&A*, 598, A7, doi: [10.1051/0004-6361/201527203](https://doi.org/10.1051/0004-6361/201527203)

Nazari, P., Tabone, B., Rosotti, G. P., et al. 2022, *A&A*, 663, A58, doi: [10.1051/0004-6361/202142777](https://doi.org/10.1051/0004-6361/202142777)

Okoda, Y., Oya, Y., Imai, M., et al. 2022, *ApJ*, 935, 136, doi: [10.3847/1538-4357/ac7ff4](https://doi.org/10.3847/1538-4357/ac7ff4)

Ospina-Zamudio, J., Lefloch, B., Ceccarelli, C., et al. 2018, *A&A*, 618, A145, doi: [10.1051/0004-6361/201832857](https://doi.org/10.1051/0004-6361/201832857)

Oya, Y., Sakai, N., Lopez-Sepulcre, A., et al. 2016, *Astrophysical Journal*, 824, 88, doi: [10.3847/0004-637x/824/2/88](https://doi.org/10.3847/0004-637x/824/2/88)

Pineda, J. E., Maury, A. J., Fuller, G. A., et al. 2012, *A&A*, 544, L7, doi: [10.1051/0004-6361/201219589](https://doi.org/10.1051/0004-6361/201219589)

Price-Whelan, A. M., Sipőcz, B. M., Günther, H. M., et al. 2018, *AJ*, 156, 123, doi: [10.3847/1538-3881/aabc4f](https://doi.org/10.3847/1538-3881/aabc4f)

Raga, A. C., Esquivel, A., Velázquez, P. F., et al. 2009, *ApJL*, 707, L6, doi: [10.1088/0004-637X/707/1/L6](https://doi.org/10.1088/0004-637X/707/1/L6)

Sabatini, G., Bianchi, E., Chandler, C. J., et al. 2025, *A&A*, 698, L16, doi: [10.1051/0004-6361/202554750](https://doi.org/10.1051/0004-6361/202554750)

Sahu, D., Liu, S. Y., Su, Y. N., et al. 2019, *Astrophysical Journal*, 872, 196, doi: [10.3847/1538-4357/aaffda](https://doi.org/10.3847/1538-4357/aaffda)

Saladino, R., Botta, G., Pino, S., Costanzo, G., & Di Mauro, E. 2012, *Chem Soc Rev*, 41, 5526, doi: [10.1039/c2cs35066a](https://doi.org/10.1039/c2cs35066a)

Santangelo, G., Codella, C., Cabrit, S., et al. 2015, *A&A*, 584, A126, doi: [10.1051/0004-6361/201526323](https://doi.org/10.1051/0004-6361/201526323)

Scibelli, S., & Shirley, Y. 2020, *ApJ*, 891, 73, doi: [10.3847/1538-4357/ab7375](https://doi.org/10.3847/1538-4357/ab7375)

Scibelli, S., Shirley, Y., Megías, A., & Jiménez-Serra, I. 2024, Monthly Notices of the Royal Astronomical Society, 533, 4104, doi: [10.1093/mnras/stae2017](https://doi.org/10.1093/mnras/stae2017)

Tang, Y.-W., Dutrey, A., Guilloteau, S., et al. 2014, ApJ, 793, 10, doi: [10.1088/0004-637X/793/1/10](https://doi.org/10.1088/0004-637X/793/1/10)

Tatematsu, K., Kim, G., Liu, T., et al. 2021, ApJS, 256, 25, doi: [10.3847/1538-4365/ac0978](https://doi.org/10.3847/1538-4365/ac0978)

Tobin, J. J., Sheehan, P. D., Megeath, S. T., et al. 2020, Astrophysical Journal, 890, 130, doi: [10.3847/1538-4357/ab6f64](https://doi.org/10.3847/1538-4357/ab6f64)

van der Wiel, M. H. D., Jacobsen, S. K., Jørgensen, J. K., et al. 2019, A&A, 626, A93, doi: [10.1051/0004-6361/201833695](https://doi.org/10.1051/0004-6361/201833695)

van 't Hoff, M. L. R., Tobin, J. J., Trapman, L., et al. 2018, ApJ, 864, L23, doi: [10.3847/2041-8213/aadb8a](https://doi.org/10.3847/2041-8213/aadb8a)

Vastel, C., Alves, F., Ceccarelli, C., et al. 2022, A&A, 664, A171, doi: [10.1051/0004-6361/202243414](https://doi.org/10.1051/0004-6361/202243414)

Velusamy, T., Langer, W. D., & Goldsmith, P. F. 2002, ApJ, 565, L43, doi: [10.1086/339246](https://doi.org/10.1086/339246)

Wang, Y.-C., Shang, H., & Krasnopolsky, R. 2025, ApJ, 987, 123, doi: [10.3847/1538-4357/add88a](https://doi.org/10.3847/1538-4357/add88a)

Yang, Y.-L., Sakai, N., Zhang, Y., et al. 2021, ApJ, 910, 20, doi: [10.3847/1538-4357/abdfd6](https://doi.org/10.3847/1538-4357/abdfd6)

Yi, H.-W., Lee, J.-E., Liu, T., et al. 2018, ApJS, 236, 51, doi: [10.3847/1538-4365/aac2e0](https://doi.org/10.3847/1538-4365/aac2e0)

Zapata, L. A., Loinard, L., Rodriguez, L. F., et al. 2013, Astrophysical Journal Letters, 764, L14, doi: [10.1088/2041-8205/764/1/L14](https://doi.org/10.1088/2041-8205/764/1/L14)